SFB/CPP-11-43
TTP11-22

# Gluino Pair Production at the LHC: The Threshold

Matthias R. Kauth, Johann H. Kühn, Peter Marquard and Matthias Steinhauser

*Institut für Theoretische Teilchenphysik*

*Karlsruhe Institute of Technology (KIT)*

*76128 Karlsruhe, Germany*

**Abstract**

The next-to-leading order analysis of the cross section of hadronic gluino pair production close to threshold is presented. Within the framework of non-relativistic QCD a significant enhancement compared to fixed order perturbation theory is observed which originates from the characteristic remnant of the $1S$ peak below the nominal pair threshold. This enhancement is similar to the corresponding one for top production. However, as a consequence of the larger colour factor of the QCD potential the effect is significantly enhanced. The analysis includes all colour configurations of $S$-wave gluino pairs, i.e. singlet, symmetric and antisymmetric octet, decuplet and twenty-seven representation. Matching coefficients involving real and virtual radiation are separately evaluated for all colour and spin configurations and initial states. We concentrate on the case of gluino decay rates comparable to the gluino binding energy. The non-relativistic dynamics of the gluino pair is solved by calculating the Green's function in NLO. Numerical results for the Large Hadron Collider at $\sqrt{s} = 14\,\text{TeV}$ and $7\,\text{TeV}$ are presented for three different, characteristic scenarios.

# 1 Introduction

The search for new particles, predicted in supersymmetric models, is one of the important tasks of the experiments at the Large Hadron Collider (LHC). The detailed determination of particle masses and couplings will be crucial for the discrimination between various manifestations of supersymmetry (SUSY) and alternative models, even more so if one wants to distinguish between the different variants of supersymmetric models, to identify the origin of breaking of supersymmetry and to measure the model parameters. One of the SUSY signals will be events with missing energy or missing transverse momentum, resulting from cascade decays of squarks and gluinos into the lightest supersymmetric particle (LSP) which escapes detection. The existence of squarks, gluinos and the LSP is definitely a key prediction of supersymmetry.

Depending on details of the models, in particular the masses of squarks and the LSP, gluinos with masses up to 3 TeV [1] could be detected. The search strategy is quite different if gluinos are heavier than squarks or if they are lighter. In the former case ($m_{\tilde{g}} > m_{\tilde{q}}$) the two-body decay into a squark and an anti-quark (or its charge conjugate) dominates, with the subsequent decay of the squark into a quark plus a chargino or neutralino. In the latter case ($m_{\tilde{g}} < m_{\tilde{q}}$) the two-body channel is kinematically forbidden and the now dominant three-body decay into quark, anti-quark and neutralino or chargino, mediated by the virtual squark, leads to a small decay rate. In the limit of extremely heavy squarks, a scenario denoted Split SUSY, the gluino is quasistable and hadrons composed of gluinos and gluons or quarks may travel macroscopic distances. The search strategies will be markedly different in the various cases.

The importance of squark and gluino searches has motivated a series of detailed studies of hadroproduction cross sections for squarks and gluinos. The lowest order has been evaluated long time ago [2–4]. Subsequently the next-to-leading order (NLO) SUSY-QCD corrections were calculated [5–7], more recently the effect of soft-gluon resummation [8–14] was included. The present paper will be concerned with gluino-pair production close to threshold, which exhibits a number of peculiar features.

As a consequence of their colour-octet representation the production cross section of gluinos is large and perturbative corrections are particularly important. Furthermore, the threshold region is strongly affected by final state interaction, which in leading order is related to Sommerfeld rescattering corrections and which, compared to the similar situation in top-anti-top production [15], is amplified by the ratio $(C_A/C_F)^2 = (9/4)^2$.

Corresponding to the different decay modes and rates, two complementary scenarios must be considered: For relatively stable gluinos (corresponding to the case $m_{\tilde{g}} < m_{\tilde{q}}$) gluino pairs may form non-relativistic boundstates, denoted gluinonia, which decay through gluino pair annihilation into a pair of gluon jets or a quark plus an anti-quark jet. This possibility has been described originally in Refs. [16–19] where the basic features like boundstate quantum numbers, leading terms in the potential, spectra and some of the production mechanisms were investigated. More recently this aspect has been studied in

Refs. [20–22]. Relatively stable gluinos are motivated by the proposal of Split SUSY [23, 24] (see also Refs. [25,26]), which suggests heavy squarks and, correspondingly, long-lived gluinos. A detailed study is presented in [27], which gives the higher order corrections to the potential, to the boundstate energy spectrum and to the production cross section for the boundstate in the colour singlet configuration.

The second scenario is relevant for gluinos with a larger decay rate, of order one GeV or higher. In this case the boundstate decay proceeds through the decay of the constituents, and for decay rates of several GeV no well defined boundstates exist. Even in this case final state interaction leads to a significant lowering of the effective production threshold, an enhancement of the cross section and a strong distortion of the differential cross section, in particular of the distribution in the invariant mass of the gluino, with details depending on the gluino mass and decay rate.

This scenario has many similarities with hadronic top quark production close to threshold [28, 29]. In particular the distribution in the invariant mass of the gluino pair can be treated with similar methods. In Ref. [30] the dominant contributions and the leading radiative corrections were classified and evaluated and a sizable enhancement of the cross section was observed. However, for a complete NLO evaluation the full ISR and hard corrections must be included. In the case of the top system these were available from the literature on the production of non-relativistic colour singlet and octet quark-anti-quark boundstates [15, 31] and could be directly applied to the case of unstable top quarks.

In contrast, the situation is more involved in the case of gluino pairs. On the one hand the production cross section depends in addition on the squark mass; for gluon induced amplitudes in NLO for quark-induced amplitudes even at tree level. On the other hand a pair of gluinos can be combined into boundstates transforming under a variety of irreducible representations partly with attractive, partly with repulsive interaction. In Ref. [30] the hard correction was extracted from the NLO result for open gluino production. However, this continuum cross section corresponds to a weighted sum of the different contributions. In the present paper these corrections will be evaluated separately for all the relevant representations, together with the individual ISR corrections. This allows to obtain the cross section including the full NLO corrections in the threshold region, the central topic of this work.

The paper will be organized as follows: For a self-contained treatment we recall in Section 2 the quantum numbers of the boundstates, discuss various SUSY scenarios and present the qualitative features of threshold production for the case of interest, i.e. for gluinos with decay rates comparable to the level spacing of the would-be boundstates.

In Section 3.1 we will present the threshold enhancement (or suppression) for the various colour configurations using Green's functions in NLO approximation. These will be evaluated similar to those of the $t\bar{t}$ system discussed in Refs. [28, 29]. In Section 3.2 the NLO pair production cross section, i.e. real and virtual corrections will be derived for the different colour and spin configurations. Only $S$ waves will be considered. Issues of renormalization, in particular the usage of dimensional reduction (DRED), and the role

| ${}^{2S+1}L_J$ | ${}^1S_0$ | ${}^3S_1$ | ${}^1P_1$ | ${}^3P_0$ | ${}^3P_1$ | ${}^3P_2$ | ${}^1D_2$ |
|---|---|---|---|---|---|---|---|
| L | 0 | 0 | 1 | 1 | 1 | 1 | 2 |
| S | 0 | 1 | 0 | 1 | 1 | 1 | 0 |
| $(\tilde{g}\tilde{g})_s$ | $0^{-+}$ | – | – | $0^{++}$ | $1^{++}$ | $2^{++}$ | $2^{-+}$ |
| $(\tilde{g}\tilde{g})_a$ | – | $1^{-+}$ | $1^{++}$ | – | – | – | – |

Table 1: Lowest-lying states $J^{PC}$ of the gluinonium spectrum. $L$ and $S$ correspond to the angular momentum and spin quantum numbers, respectively.

of virtual gluino or squark pairs will be discussed, together with the choice of the proper value of the strong coupling $\alpha_s$.

Using this input, the hadronic production cross section can be evaluated in a straightforward way in Section 4. We will limit the discussion to proton-proton collisions at 7 and 14 TeV and give results for several of the SUSY scenarios discussed in Section 2. Section 5 contains our conclusions. Appendix A contains useful relations for the generalized hypergeometric function ${}_4F_3$, and some of the longer formulae are relegated to Appendix B. In Appendix C details of the benchmark scenarios used in this paper are provided.

# 2 SUSY scenarios, gluino boundstates and threshold behaviour

Let us briefly recall the quantum numbers of gluino pairs in the threshold region, classified according to their colour, spin and orbital momentum configurations [16–18]. They differ from those of quark-anti-quark states due to the restrictions arising from the Majorana nature of gluinos, and due to their different colour assignment.

Two colour-octet states can be combined into irreducible representations as follows (see e.g. [32])

$$8 \otimes 8 \;=\; 1_s \oplus 8_s \oplus 8_a \oplus 10_a \oplus \overline{10}_a \oplus 27_s \,, \tag{1}$$

where the subscript indicates (anti-)symmetry with respect to their colour index. Fermi statistics and the Majorana nature of the gluinos lead to additional restrictions. For the symmetric colour configurations $1_s$, $8_s$ and $27_s$ antisymmetric spin-angular momentum wave functions, $(-1)^{L+S} = 1$, are required, for the antisymmetric colour configurations $8_a$, $10_a$ and $\overline{10}_a$ symmetric ones, $(-1)^{L+S} = -1$. The intrinsic parity of a Majorana particle can be chosen to be imaginary, its parity under charge reflection real, leading to negative intrinsic parity and positive charge parity of the boundstate. For a few lowest orbital angular momenta the complete set of boundstate quantum numbers is listed in Tab. 1. Restricting ourselves to the near threshold region, only $S$-wave configurations will be retained.

| R | $(F^R)^2$ | $F^{a,1}\cdot F^{a,2}$ | interaction |
|---|---|---|---|
| $1_s$ | 0 | $-3$ | attractive |
| $8_s, 8_a$ | 3 | $-\frac{3}{2}$ | attractive |
| $10_a, \overline{10}_a$ | 6 | 0 | neutral |
| $27_s$ | 8 | 1 | repulsive |

Table 2: Colour interaction of two SU(3) octets.

Depending on the representation $R$ of the boundstate, the interaction between the two gluinos can be either attractive, repulsive or absent (in lowest order). In lowest order the coefficient $C^{[R]}$ of the QCD potential which governs the final state interaction is given by the expectation value of the product of the colour generators $F^a_{ij}F^a_{kl}$, taken between two-particle states in the respective representation. This product, in turn, can be expressed by the eigenvalues of the quadratic Casimir operator of the constituents, $C_A = 3$, and the boundstate in representation $R$, $C_R = \left(F^R\right)^2$:

$$C^{[R]} \;\equiv\; F^{a,1}\cdot F^{a,2} \;=\; \frac{1}{2}\left[(F^R)^2 - (F^{a,1})^2 - (F^{a,2})^2\right] = \frac{1}{2}\left(C_R - 2C_A\right) . \qquad (2)$$

The results are listed in Tab. 2. For the cases with negative (positive) coefficients, corresponding to attraction (repulsion), the cross section will be enhanced (suppressed). Also the NLO correction of the QCD potential, which will be needed below, is proportional to the same group theoretical factor [30]. The classification described in Tabs. 1 and 2 is of course also applicable to continuum production and will be important for the description of final state interaction.

As mentioned in the Introduction and discussed in the literature [16–18, 27, 30] the phenomenology of gluino pair production in the threshold region is governed by the relative size of the decay rate of a gluino, $\Gamma_{\tilde{g}}$, compared to the rate for gluinonium annihilation into gluons, $\Gamma_{gg}$, on the one hand, and by the relative size of $\Gamma_{\tilde{g}}$ and the level spacing $\Delta M$ between the ground state and the first radial excitation of the colour singlet boundstate on the other hand. Specifically we adopt for this comparison the single-gluino decay rate of the boundstate, corresponding to $2\Gamma_{\tilde{g}}$. The choice of $\Delta M = |E_1 - E_2|$ is motivated by the fact that the binding energy per se depends evidently on the choice of the mass definition (pole mass, potential subtracted mass, ...) while $\Delta M$ is convention independent.

If the decay rate $2\Gamma_{\tilde{g}}$ is smaller than the annihilation rate of the ($S$-wave) boundstate, which in lowest order is approximately given by $\Gamma_{gg} \approx C_A^2\alpha_s^2\,|R(0)|^2/(2m_{\tilde{g}}^2) \approx (C_A\alpha_s)^5 m_{\tilde{g}}/4$, the signatures of boundstate and open gluino production are distinctively different: Boundstates produced below the pair threshold decay into two gluon jets (no missing energy), in contrast to the complicated cascade decays of gluinos above threshold. This case (class A), evidently true in Split SUSY, was discussed in detail in Ref. [27], with emphasis on the production of colour singlet boundstates.

If $\Gamma_{gg} \lesssim 2\Gamma_{\tilde{g}}$, the constituents decay before they can annihilate and the qualitative decay signatures of bound and unbound gluinos are practically indistinguishable. Nevertheless, the distribution in the invariant mass of the gluino pair will still be modulated and strongly affected by final state interaction. As long as $2\Gamma_{\tilde{g}} < \Delta M$, this mass distribution will still reflect the presence of the boundstates, at least the enhancement resulting from the lowest $1S$ resonance with quantum numbers $0^{-+}$ (class B). For even larger gluino decay rates i.e. $2\Gamma_{\tilde{g}} \geq \Delta M$ these structures have essentially disappeared resulting in an unstructured threshold behaviour (class C). Nevertheless the cross section is still modified by final state interaction and receives a significant contribution from the region below threshold as far as colour singlet and octet rates are concerned and a sizable suppression for the 27 representation.

The dependence of $\Gamma_{gg}$, $2\Gamma_{\tilde{g}}$ and $\Delta M$ on $m_{\tilde{g}}$ is illustrated in Fig. 1. In Fig. 1a we compare $\Delta M$ and $\Gamma_{gg}$, evaluated in NLO [27], to the decay rate $2\Gamma_{\tilde{g}}$, evaluated for three generic choices of squark masses 0.5 TeV, 1.0 TeV and 1.5 TeV. In Fig. 1b fixed ratios between $m_{\tilde{g}}$ and $m_{\tilde{q}}$ ($m_{\tilde{g}}/m_{\tilde{q}}$ = 0.75, 0.90, 1.05, 1.25) are adopted. In Tab. 5 (Appendix C) we define 17 benchmark points on the basis of various SPS scenarios introduced in Ref. [33]. Decay rates and SUSY masses corresponding to our benchmark points are calculated with the programs `SuSpect` [34] and `SDECAY` [35]. The essential information, i.e. gluino mass, averaged squark mass, level spacing of gluinonium, gluino decay rate, gluinonium annihilation decay and dominant gluino decay channels, is listed in Tab. 3. Tabs. 6 and 7 in Appendix C contain detailed information on the squark masses of the benchmark points. Gluino masses and decay rates, level spacing and annihilation rate of gluinonium for these benchmark points are shown in Fig. 1c. It is clear from this figure and Tab. 3, that all three possibilities, corresponding to class A, B and C could arise and should be discussed. Note, that even the three cases which fall into class C are fairly close to the boundary between B and C, such that a structured threshold behaviour is typical for all benchmark points discussed in this paper.

Class A has been studied in detail in [27], with emphasis on colour singlet production. The present paper will be concerned with class B, with results also applicable to class C.

Let us now recall the qualitative aspects of the production mechanism. Similar to the case of top quark production [28, 29] (see also [36]) the cross section for a bound state $T$, differential in $M$, the invariant mass of the gluino pair, can be decomposed into a factor representing the hard, short distance part of the production process, and a factor given by the imaginary part of the Green's function evaluated at the origin and the convolution with the luminosity functions

$$M\frac{\mathrm{d}\sigma_{PP\to T}}{\mathrm{d}M}(S,M^2) \;=\; \sum_{i,j}\int_{\rho}^{1}\mathrm{d}\tau\,\left[\frac{\mathrm{d}\mathcal{L}_{ij}}{\mathrm{d}\tau}\right](\tau,\mu_F^2)M\frac{\mathrm{d}\hat{\sigma}_{ij\to T}}{\mathrm{d}M}(\hat{s},M^2,\mu_R^2,\mu_F^2)\,, \qquad (3)$$

(a)

(b)

(c)

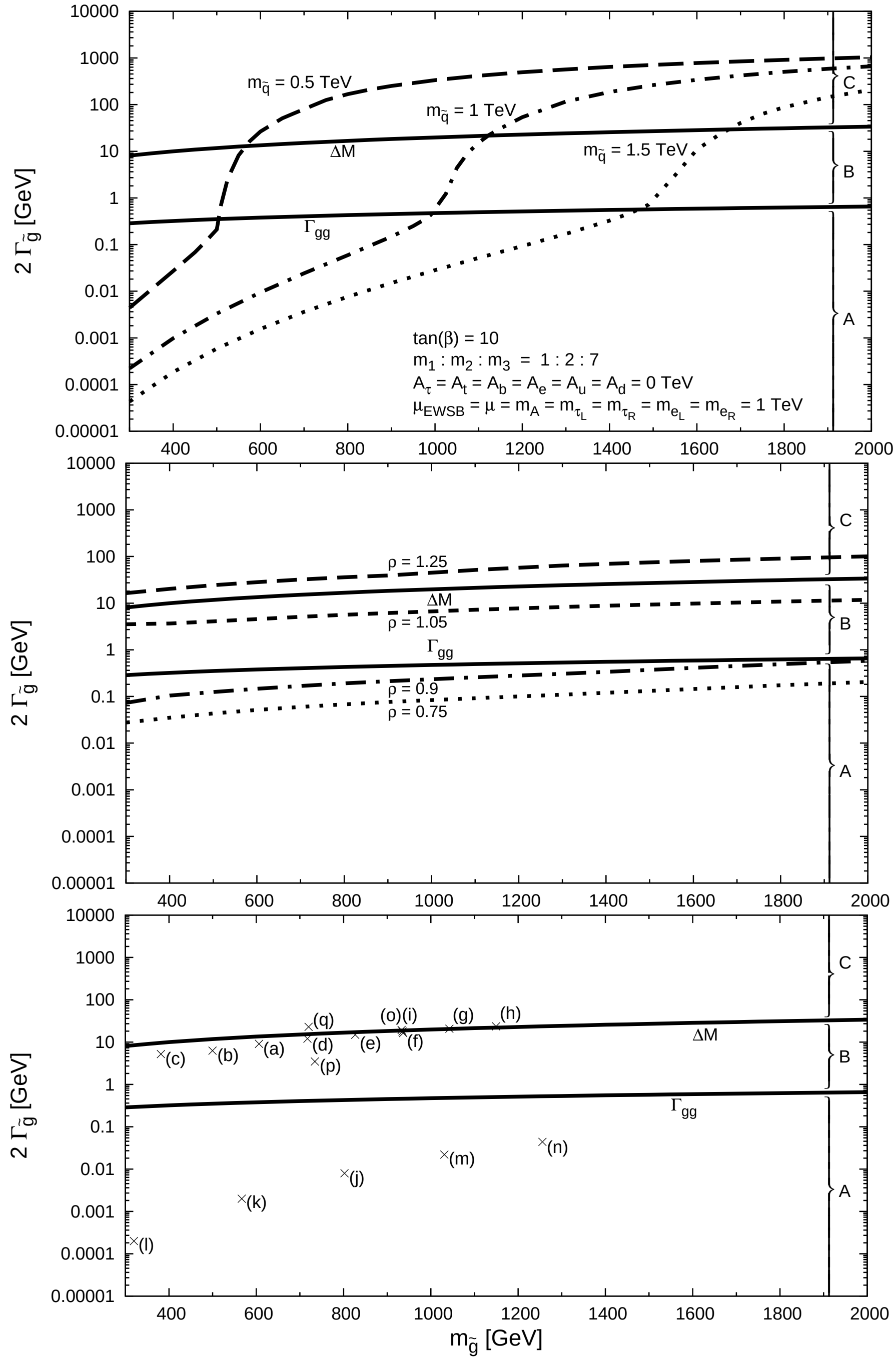


Figure 1: Level spacing $\Delta M$ and annihilation rates $\Gamma_{gg}$ (solid curves) compared to the gluino decay rates $2\Gamma_{\tilde{g}}$. Fig. (a): for three different squark masses (dashed: 0.5 TeV, dash-dotted: 1 TeV, dotted: 1.5 TeV). Fig. (b): for fixed ratios ($\rho = m_{\tilde{g}}/m_{\tilde{q}}$) between squark and gluino masses. Fig. (c): for the benchmark points (see Tab. 3).

| benchmark point | $m_{\tilde{g}}$ [GeV] | $\overline{m}_{\tilde{q}}$ [GeV] | $\Delta M$ [GeV] | $2\Gamma_{\tilde{g}}$ [GeV] | $\Gamma_{gg}$ [GeV] | class | dominant decay channels |
|---|---|---|---|---|---|---|---|
| (a) | 606.11 | 541.04 | 13.89 | 9.08 | 0.37 | $B$ | $\tilde{g} \to \tilde{b}_1\overline{b}, \tilde{b}_1^*b$ |
| (b) | 493.05 | 443.19 | 12.04 | 6.28 | 0.34 | $B$ | $\tilde{g} \to \tilde{c}_2\overline{c}, \tilde{c}_2^*c,$ $\tilde{u}_2\overline{u}, \tilde{u}_2^*u$ |
| (c) | 381.45 | 344.04 | 9.88 | 5.20 | 0.30 | $B$ | $\tilde{g} \to \tilde{b}_1\overline{b}, \tilde{b}_1^*b$ |
| (d) | 717.12 | 637.39 | 15.75 | 12.00 | 0.40 | $B$ | $\tilde{g} \to \tilde{b}_1\overline{b}, \tilde{b}_1^*b$ |
| (e) | 826.71 | 732.62 | 17.52 | 14.92 | 0.43 | $B$ | $\tilde{g} \to \tilde{t}_1\overline{t}, \tilde{t}_1^*t$ |
| (f) | 935.18 | 826.94 | 19.22 | 17.84 | 0.46 | $B$ | $\tilde{g} \to \tilde{b}_1\overline{b}, \tilde{b}_1^*b$ |
| (g) | 1042.60 | 920.35 | 20.87 | 20.70 | 0.48 | $B$ | $\tilde{g} \to \tilde{t}_1\overline{t}, \tilde{t}_1^*t$ |
| (h) | 1149.42 | 1013.25 | 22.47 | 23.52 | 0.51 | $C$ | $\tilde{g} \to \tilde{t}_1\overline{t}, \tilde{t}_1^*t$ |
| (i) | 936.42 | 831.88 | 19.24 | 16.38 | 0.46 | $B$ | $\tilde{g} \to \tilde{b}_1\overline{b}, \tilde{b}_1^*b$ |
| (j) | 802.21 | 1462.40 | 17.13 | 0.0080 | 0.43 | $A$ | $\tilde{g} \to \tilde{\chi}_2^+b\overline{t}, \tilde{\chi}_2^-t\overline{b}$ |
| (k) | 566.65 | 1219.50 | 13.21 | 0.0020 | 0.36 | $A$ | $\tilde{g} \to \tilde{\chi}_2^0b\overline{b}$ |
| (l) | 319.59 | 987.34 | 8.69 | 0.0002 | 0.28 | $A$ | $\tilde{g} \to \tilde{\chi}_1^+d\overline{u}, \tilde{\chi}_1^-u\overline{d},$ $\tilde{\chi}_1^+s\overline{c}, \tilde{\chi}_1^-c\overline{s}$ |
| (m) | 1030.98 | 1710.01 | 20.69 | 0.022 | 0.48 | $A$ | $\tilde{g} \to \tilde{\chi}_2^+b\overline{t}, \tilde{\chi}_2^-t\overline{b}$ |
| (n) | 1255.61 | 1959.83 | 24.04 | 0.044 | 0.53 | $A$ | $\tilde{g} \to \tilde{\chi}_2^+b\overline{t}, \tilde{\chi}_2^-t\overline{b}$ |
| (o) | 933.03 | 819.58 | 19.19 | 19.26 | 0.46 | $C$ | $\tilde{g} \to \tilde{t}_1\overline{t}, \tilde{t}_1^*t$ |
| (p) | 734.11 | 714.46 | 16.02 | 3.48 | 0.41 | $B$ | $\tilde{g} \to \tilde{b}_1\overline{b}, \tilde{b}_1^*b$ |
| (q) | 719.66 | 618.86 | 15.79 | 22.92 | 0.40 | $C$ | $\tilde{g} \to \tilde{t}_1\overline{t}, \tilde{t}_1^*t$ |

Table 3: Comparison of gluino masses, average squark masses, gluinonium level spacing, single decay rate, annihilation rate and dominant decay channels for the 17 benchmark points defined in Appendix C, Tab. 5.

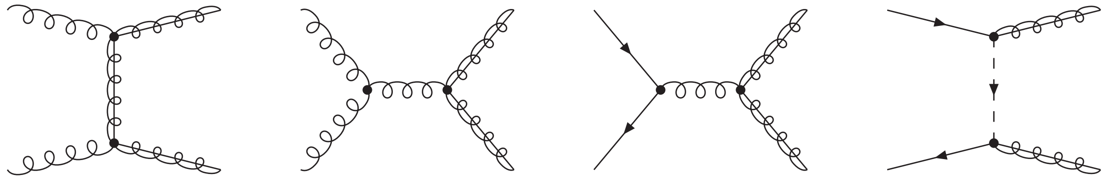

Figure 2: Feynman diagrams contributing at LO to $gg \to \tilde{g}\tilde{g}$ and $q\overline{q} \to \tilde{g}\tilde{g}$.

with

$$\begin{aligned} M\frac{\mathrm{d}\hat{\sigma}_{ij\to T}}{\mathrm{d}M}(\hat{s}, M^2, \mu_R^2, \mu_F^2) &= \mathcal{F}_{ij\to T}(\hat{s}, M^2, \mu_R^2, \mu_F^2)\frac{1}{m_{\tilde{g}}^2}\mathrm{Im}\left\{G^{[1,8,10,27]}(0, M-2m_{\tilde{g}}+i\Gamma_{\tilde{g}})\right\} , \\ \left[\frac{\mathrm{d}\mathcal{L}_{ij}}{\mathrm{d}\tau}\right](\tau, \mu_F^2) &= \int_0^1 \mathrm{d}x_1 \int_0^1 \mathrm{d}x_2 f_{i|P}(x_1, \mu_F^2) f_{j|P}(x_2, \mu_F^2)\delta(\tau - x_1x_2) . \end{aligned} \tag{4}$$

As usual $\hat{s}$ and $S$ denote the partonic and the hadronic center-of-mass energy squared, respectively, and $\tau = \hat{s}/S$. The lower limit of the $\tau$ integration is given by $\rho = M^2/S$. The superscript of the Green's function refers to the colour state of $T$ and $\mu_F$ and $\mu_R$ denote the factorization and renormalization scale.

In leading order (LO) gluino pairs can be produced by gluon fusion or quark-anti-quark annihilation (Fig. 2), at NLO also the quark-gluon channel contributes.

The strength of final state interaction at threshold is determined by the respective colour representation of the gluino pair. To disentangle the different representations it is convenient to use the following projectors [37]

$$\begin{aligned} \mathbb{P}_{1_S}^{ab,cd} &= \frac{1}{8}\delta_{ab}\delta_{cd} , \\ \mathbb{P}_{8_S}^{ab,cd} &= \frac{3}{5}d_{abe}d_{cde} , \\ \mathbb{P}_{8_A}^{ab,cd} &= \frac{1}{3}f_{abe}f_{cde} , \\ \mathbb{P}_{10}^{ab,cd} &= \frac{1}{2}\left(\delta_{ac}\delta_{bd} - \delta_{ad}\delta_{bc}\right) - \frac{1}{3}f_{abe}f_{cde} , \\ \mathbb{P}_{27_S}^{ab,cd} &= \frac{1}{2}\left(\delta_{ac}\delta_{bd} + \delta_{ad}\delta_{bc}\right) - \frac{3}{5}d_{abe}d_{cde} - \frac{1}{8}\delta_{ab}\delta_{cd} , \end{aligned} \tag{5}$$

where $\mathbb{P}_{10}$ is the projector on $10_a \oplus \overline{10}_a$ and

$$\begin{aligned} \delta_{ac}\delta_{bd}\mathbb{P}_X^{ab,cd} &= N_X , \\ \mathbb{P}_X^{ab,cd}\mathbb{P}_Y^{cd,ef} &= \delta_{XY}\mathbb{P}_X^{ab,ef} , \\ \sum_X \mathbb{P}_X^{ab,cd} &= \delta_{ac}\delta_{bd} . \end{aligned} \tag{6}$$

The normalization constant $N_X$ is given by the dimension of the representation $X$, where $N_{10} = N_{10_a} + N_{\overline{10}_a} = 20$. As stated above, colour representation, spin and orbital angular momentum of the gluino pair are interlocked. $S$-wave gluino pairs in symmetric and anti-symmetric colour configurations combine into spin singlet and triplet states, respectively. For the quantities $\mathcal{F}_{ij\to T}$ (as introduced in Eq. (4)) describing the hard kernel one finds in Born approximation

$$\mathcal{F}^{(0)}_{ij\to T} = \mathcal{N}^{[T]}_{ij} \frac{9\pi^2 \alpha_s^2(\mu_R)}{4\hat{s}} \delta(1-z) \ , \tag{7}$$

with the non-vanishing normalization factors

$$\begin{aligned} \mathcal{N}^{[T]}_{gg} &= 1,2,3 \quad \text{for} \quad T = 1_s, 8_s, 27_s \ , \\ \mathcal{N}^{[8_a]}_{q\overline{q}} &= \frac{128}{27}\left(\frac{r-1}{r+1}\right)^2 \ . \end{aligned} \tag{8}$$

Here $z = M^2/\hat{s}$ and $r = \overline{m}^2_{\tilde{q}}/m^2_{\tilde{g}}$ where $\overline{m}_{\tilde{q}}$ is the averaged squark mass as introduced in Tab. 3. The Green's function which depends on the energy $E = M - 2m_{\tilde{g}}$ and the decay rate of the gluino $\Gamma_{\tilde{g}}$ is obtained from the Schrödinger equation

$$\left\{ \left[ \frac{(-i\nabla)^2}{m_{\tilde{g}}} + V_C^{[1,8,10,27]}(\vec{r}) \right] - (E + i\Gamma_{\tilde{g}}) \right\} G^{[1,8,10,27]}(\vec{r}, E + i\Gamma_{\tilde{g}}) = \delta^{(3)}(\vec{r}) \tag{9}$$

with the "Coulomb" potential $V_C^{[R]}(\vec{r}) = -C^{[R]}\alpha_s(\mu_R)/r$ (and $C^{[R]} = 3, 3/2, 0, -1$ for $R = 1, 8, 10, 27$) in lowest order. NLO corrections to the hard kernel, the potential and the Green's function will be discussed in the next section, numerical results will be presented for a variety of scenarios in Section 4. From now on we shall limit our discussion to three typical benchmark points (p), (a) and (q) (see Fig. 1 and Tab. 3). For (p), due to the close proximity of squark and gluino masses, the decay rate of the boundstate, which is approximately $2\Gamma_{\tilde{g}}$, is significantly lower than $\Delta M$ and, as a consequence, the enhancement from the lowest lying resonances is well visible. This is the case we will discuss in most detail. The other two points serve to illustrate the case of gluinos with somewhat larger decay rates.

The imaginary parts of the LO and NLO Green's functions (for $R = 1, 8, 10, 27$) are displayed in Fig. 3(a). We have adopted twice the Bohr radius as characteristic scale in $\alpha_s$ for the attractive potential, $\alpha_s(M_Z) = 0.1202$ as starting value and two-loop running. This leads to $\alpha_s^{[R]} = \alpha_s(C^{[R]}\alpha_s^{[R]} m_{\tilde{g}}) = \{0.1034, 0.1124\}$ for $[R] = 1, 8$ and $\alpha_s^{[27]} = \alpha_s(\left|C^{[27]}\right| \alpha_s^{[27]} m_{\tilde{g}}) = 0.1184$ for the repulsive potential of the twenty-seven representation. Two further characteristic examples are shown in Figs. 3(b) and (c) corresponding to benchmark points (a) and (q) with significantly larger $\Gamma_{\tilde{g}}$. LO and NLO predictions are shown for the singlet (dashed) and for the octet configuration (dash-dotted), anticipating the results of Section 3.1. In our approximation the potential of the decuplet vanishes and thus the free Green's function is shown (solid). For the repulsive twenty-seven configuration the NLO corrections are quite small, i.e. LO and NLO

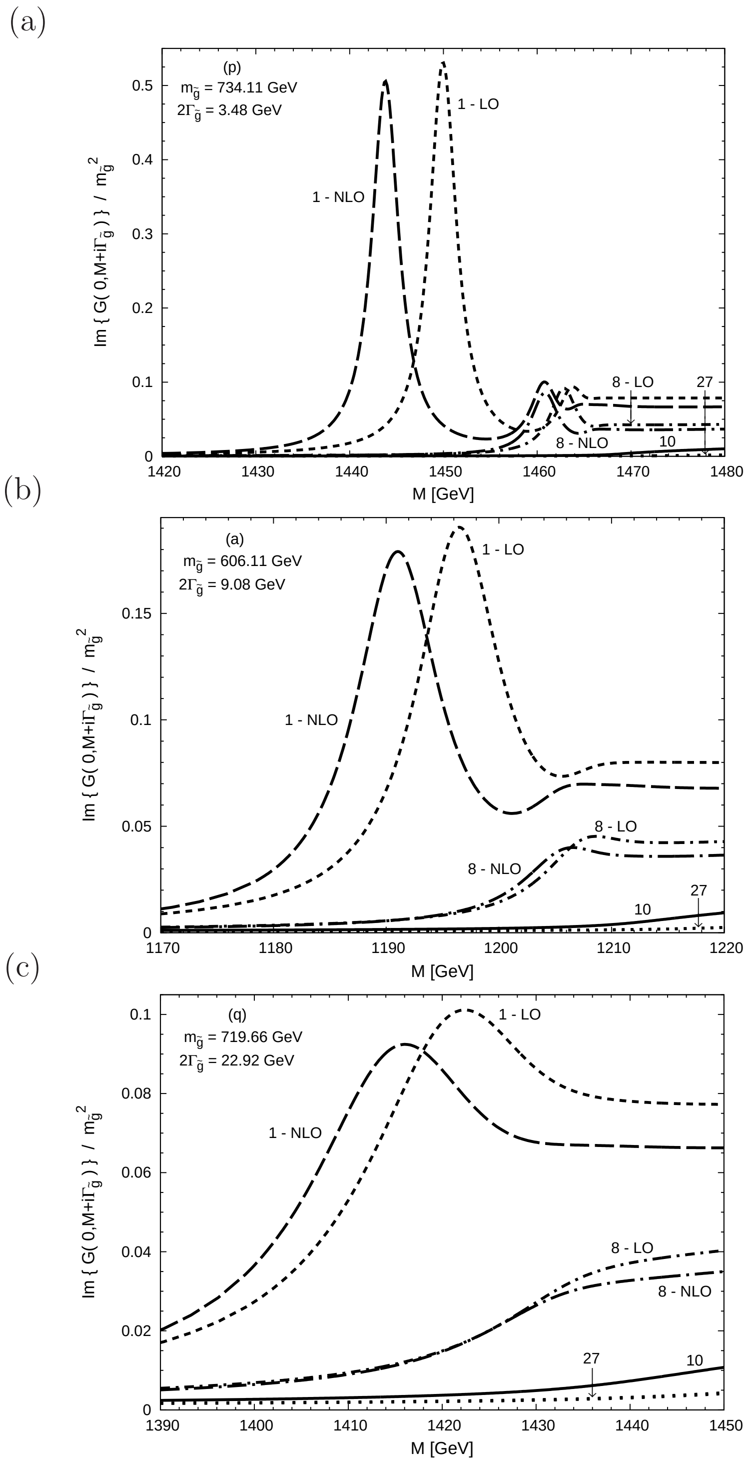


Figure 3: Imaginary part of the Green's functions for benchmark points (p), (a) and (q) for the singlet (dashed), octet (dash-dotted), decuplet (solid) and twenty-seven configuration (dotted). For the decuplet we show the free Green's function. LO and NLO curves for twenty-seven lie on top of each other.

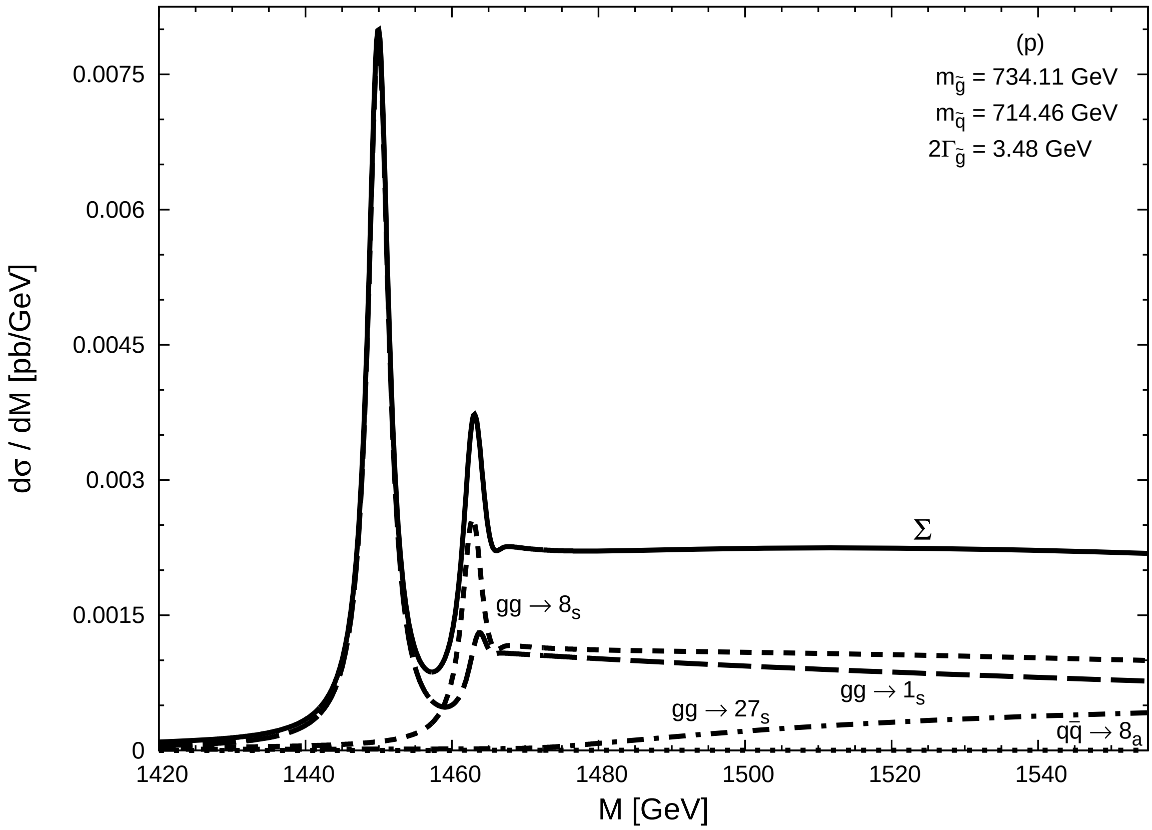


Figure 4: LO prediction for the invariant mass distribution for scenario (p).

nearly coincide. The accidental near degeneracy of the first radial excitation from $G^{[1]}$ with the lowest enhancement of $G^{[8]}$ follows trivially from the ratio between the strengths of potential $(C^{[8]}/C^{[1]})^2 = 1/4$ and the excitation spectrum for the Coulomb potential, $E_n \sim 1/n^2$. For (p) the lowest resonances are still nicely separated, for (q), which is close to the border between class B and C (see Fig. 1(c)), individual resonances have nearly disappeared. Nevertheless final state interaction leads to a significant modification of the threshold behaviour and to marked differences between the different colour representations. The Green's functions for symmetric and antisymmetric octet are obviously identical and denoted by $G^{[8]}$, the difference between the two states is only the spin configuration.

The LO prediction for the cross section is shown in Fig. 4 separately for the four different contributions and the sum. We have employed the PDF set MSTW2008LO [38] which fixes the value $\alpha_s(M_Z) = 0.1394$. We use two-loop running and one-loop decoupling (as implemented in the program `RunDec` [39]) to obtain the strong $\overline{\rm MS}$ coupling at the scale $\mu = 2m_{\tilde{g}}$. In a next step we transform the coupling to the $\overline{\rm DR}$ scheme in the full SUSY QCD theory with one-loop approximation (see, e.g., Ref. [40]). Note, that the $q\overline{q}$ induced production of $8_a$ is strongly suppressed as a consequence of the destructive interference between the amplitudes with $s$-channel gluon and $t$- as well as $u$-channel squark exchange and the near degeneracy of squark and gluino masses

$$\frac{\mathcal{F}_{q\bar{q}\to 8_a}}{\mathcal{F}_{gg\to 1_s}} = \frac{128}{27}\left(\frac{m_{\tilde{g}}^2 - m_{\tilde{q}}^2}{m_{\tilde{g}}^2 + m_{\tilde{q}}^2}\right)^2 \cong 3.5\cdot 10^{-3}, 6.1\cdot 10^{-2}, 1.1\cdot 10^{-1}\,, \tag{10}$$

for the benchmark points (p), (a), (q). Close to threshold the repulsive final state interaction of $27_s$ leads to a strong suppression of the cross section. For larger energies this effect disappears quickly as a consequence of the large multiplicity of states in the $27_s$ representation.

# 3 Next-to-leading order corrections

The NLO corrections to the cross section, whose evaluation is the main subject of this work, can be separated into those for the Green's function $\mathrm{Im}\,\{G(0, E + i\Gamma_{\tilde{g}})\}$ and those for the hard coefficients $\mathcal{F}_{ij\to T}$, as defined in Eq. (4).

## 3.1 Green's function

Following the idea of the Green's function formalism developed in Refs. [41–43] we start with using the NLO potential in momentum space[1]

$$\widetilde{V}_C^{[R]}(\vec{q}) = -C^{[R]}\frac{4\pi\alpha_s(\mu_G)}{\vec{q}^{\,2}}\left[1 + \frac{\alpha_s(\mu_G)}{4\pi}\left(\beta_0 \ln\frac{\mu_G^2}{\vec{q}^{\,2}} + a_1\right)\right]\,, \tag{11}$$

with [18]

$$\begin{aligned} C^{[1]} &= C_A = 3\,, \\ C^{[8]} &= \frac{1}{2}C_A = \frac{3}{2}\,, \\ C^{[10]} &= 0\,, \\ C^{[27]} &= -\frac{1}{3}C_A = -1\,, \end{aligned} \tag{12}$$

and

$$\begin{aligned} a_1 &= \frac{31}{9}C_A - \frac{20}{9}T_F n_f\,, \\ \beta_0 &= \frac{11}{3}C_A - \frac{4}{3}T_F n_f\,. \end{aligned} \tag{13}$$

[1]For colour triplet or octet states combined into singlet boundstates the potential is even known to NNNLO [44–47], for the combination of colour triplet states into octet representations see [48].

We have checked by an explicit calculation that for all colour configurations the same coefficient $a_1$ is obtained. The renormalization scale relevant for potential and Green's function is denoted by $\mu_G$ and chosen to be the solution of $\mu_G = \left|C^{[R]}\right| \alpha_s(\mu_G) m_{\tilde{g}}$. The strong coupling is defined in the $\overline{\text{MS}}$ scheme and for five active flavours. In principle one might include top-quark mass effects, however, at the present level of precision these terms are still irrelevant and are neglected in the potential.

The Green's function for the top-anti-top system is known in compact analytic form [49] (see also [50]) and the result is easily applied to the present case

$$G^{[R]}(0, M - 2m_{\tilde{g}} + i\Gamma_{\tilde{g}}) \;=\; i\frac{v m_{\tilde{g}}^2}{4\pi} + \frac{C^{[R]}\alpha_s(\mu_G) m_{\tilde{g}}^2}{4\pi}\left[g_{\text{LO}} + \frac{\alpha_s(\mu_G)}{4\pi} g_{\text{NLO}} + \ \ldots\right], \tag{14}$$

with

$$\begin{aligned} g_{\text{LO}} &\equiv L - \psi^{(0)}\,, \\ g_{\text{NLO}} &\equiv \beta_0 \bigg[ L^2 - 2L\left(\psi^{(0)} - \kappa\psi^{(1)}\right) + \kappa\psi^{(2)} + \left(\psi^{(0)}\right)^2 - 3\psi^{(1)} - 2\kappa\psi^{(0)}\psi^{(1)} \\ &\qquad + 4\, {}_4F_3\left(1,1,1,1;2,2,1-\kappa;1\right)\bigg] + a_1\left[L - \psi^{(0)} + \kappa\psi^{(1)}\right], \end{aligned} \tag{15}$$

and

$$\begin{aligned} \kappa &\equiv i\frac{C^{[R]}\alpha_s(\mu_G)}{2v}\,, \\ v &\equiv \sqrt{\frac{M - 2m_{\tilde{g}} + i\Gamma_{\tilde{g}}}{m_{\tilde{g}}}}\,, \\ L &\equiv \ln\frac{i\mu_G}{2m_{\tilde{g}} v}\,. \end{aligned} \tag{16}$$

The $n$-th derivative $\psi^{(n)} = \psi^{(n)}(1-\kappa)$ of the digamma function $\psi(z) = \gamma_E + (d/dz)\ln\Gamma(z)$ is evaluated at $(1-\kappa)$ and the Generalized Hypergeometric Function ${}_4F_3$ is defined in Appendix A.

Solving the Schrödinger equation perturbatively induces poles in the Green's function of the form $\left\{\alpha_s E_n^{\text{LO}} / \left[E_n^{\text{LO}} - (E + i\Gamma_{\tilde{g}})\right]\right\}^k$ which become large in the vicinity of $E = E_n^{\text{LO}}$ for a small decay width $\Gamma_{\tilde{g}}$. To obtain a proper Green's function with single poles one has to resum the multiple poles as proposed in [49] by adding the term

$$\begin{aligned} &\frac{F_n^{\text{LO}}\left(1 + \alpha_s f_1\right)}{E_n^{\text{LO}}(1 + e_1\alpha_s) - (E + i\Gamma_{\tilde{g}})} \\ &- \left\{ \frac{F_n^{\text{LO}}}{E_n^{\text{LO}} - (E + i\Gamma_{\tilde{g}})} + \alpha_s\left[ -\frac{F_n^{\text{LO}} E_n^{\text{LO}} e_1}{\left(E_n^{\text{LO}} - (E + i\Gamma_{\tilde{g}})\right)^2} + \frac{F_n^{\text{LO}} f_1}{E_n^{\text{LO}} - (E + i\Gamma_{\tilde{g}})}\right]\right\}, \end{aligned} \tag{17}$$

which is of order $\alpha_s^2$. The Schrödinger wave function at the origin as well as the binding energy are given by $|\Psi_n(0)|^2 = F_n^{\rm LO}\,(1+\alpha_s f_1+\dots)$ and $E_n = E_n^{\rm LO}\,(1+\alpha_s e_1+\dots)$. The quantities $F_n^{\rm LO}$, $E_n^{\rm LO}$, $f_1$ and $e_1$ can be found in Appendix A of Ref. [27].

Attention has to be paid to the numerical evaluation of the Generalized Hypergeometric Function ${}_4F_3$ in Eq. (14). This function has a branch cut for its last argument on the real positive axis starting from 1. Hence the series defining this function converges for $\mathrm{Re}\,(1-\kappa) > 1$, a condition potentially violated[2] for small $|E + i\Gamma_{\tilde{g}}|$. In Appendix A it is shown how to circumvent this problem by a suitable transformation.[3]

Due to the factorization, formulated in Eq. (3), the renormalization scales of Green's function $\mu_G$ and short distance part $\mu_R$, appearing below, can be chosen independently. For our choice of $\mu_G$, twice the inverse of the Bohr radius of the two gluino system, the Coulomb-Green's function has a well convergent perturbative series as discussed in Ref. [51] for the top-anti-top pair in the colour-singlet configuration.

## 3.2 Short distance corrections

The calculation of the partonic cross sections has been performed in dimensional regularization (DREG). The Feynman diagrams have been generated using FeynArts [52,53], for the evaluation we have used in-house FORM [54] programs and FormCalc [53]. Masses and wavefunctions are renormalized on-shell while minimal subtraction ($\overline{\rm MS}$) is used for the coupling. DREG violates supersymmetry because of a mismatch of the degrees of freedom of the gauge bosons and their fermionic superpartners. This problem has been resolved by introducing dimensional reduction (DRED) [55] as regularization method where the elegant features of DREG are maintained. While the on-shell masses do not depend on the choice of scheme the coupling has now to be calculated in DRED combined with minimal subtraction, the so-called $\overline{\rm DR}$ scheme. The transition between the $\overline{\rm MS}$ and $\overline{\rm DR}$ parameters is known up to two loops [56,57]. For our calculation the one-loop relations are sufficient which we need for the Yukawa coupling, which appears in the gluino-quark-squark vertices, and the gauge coupling in the three-gluon, gluon-quark and gluon-gluino vertices. Our final results are expressed in terms of $\alpha_s^{\overline{\rm DR}} \equiv \alpha_s^{(\rm SQCD)}$, the strong SUSY QCD coupling in the $\overline{\rm DR}$ scheme.

The corresponding amplitudes have to be projected onto the proper spin configuration [58,59] and the corresponding colour representation (see Eq. (5)). As discussed in Section 2 the colour-symmetric configurations (with $L = 0$) have spin $S = 0$, the antisymmetric ones $S = 1$. For the processes, which are non-vanishing in Born approximation, the hard part of the partonic cross sections can be written in the form (with the factors $\mathcal{N}_{ij}^{[T]}$ given

[2]The condition is fulfilled for $1 > \left|E_1^{\rm LO}\right| \left(\sqrt{E^2+\Gamma^2} - E\right) / \left[2(E^2+\Gamma^2)\right]$. Hence this problem does not arise for the $t\bar{t}$ system.

[3]We thank Yuichiro Kiyo for communications concerning this point.

in Eq. (8))

$$\mathcal{F}_{ij\to T} \;=\; \mathcal{N}_{ij}^{[T]}\frac{9\pi^2\left(\alpha_s^{\overline{\mathrm{DR}}}(\mu_R)\right)^2}{4\hat{s}}\left(1+\frac{\alpha_s^{\overline{\mathrm{DR}}}(\mu_R)}{\pi}\overline{\mathcal{V}}_{ij}^{[T]}\right)\left[\delta(1-z)+\frac{\alpha_s^{\overline{\mathrm{DR}}}(\mu_R)}{\pi}\overline{\mathcal{R}}_{ij}^{[T]}(z)\right]. \tag{18}$$

The remaining ones are given by

$$\mathcal{F}_{ij\to T} \;=\; \frac{9\pi\left(\alpha_s^{\overline{\mathrm{DR}}}(\mu_R)\right)^3}{4\hat{s}}\overline{\mathcal{R}}_{ij}^{[T]}(z)\,. \tag{19}$$

Furthermore, $\mathcal{F}_{g\bar{q}\to T}$ is equal to $\mathcal{F}_{gq\to T}$. The quantities $\overline{\mathcal{V}}_{ij}^{[T]}$ and $\overline{\mathcal{R}}_{ij}^{[T]}$ denote the virtual and real corrections and are obtained from the results listed below (see Eqs. (20) – (24)) by dropping the infrared singularities, which cancel between $\mathcal{V}_{ij}^{[T]}$ and $\mathcal{R}_{ij}^{[T]}$. For the Born approximation in $d=4-2\varepsilon$ dimensions a factor $(1-\varepsilon)(1-2\varepsilon)$ for the pseudoscalar and $(1-\varepsilon)$ for the vector states has been taken into account. (Note that collinear singularities from $\mathcal{R}_{ij}^{[T]}$ are already absorbed in the PDFs.)

The only non-vanishing contributions to the hard virtual corrections read

$$\begin{aligned}\mathcal{V}_{gg}^{[1_s]} \;=\;& \Bigg\{-\frac{3}{\varepsilon_{\mathrm{IR}}^2}-\frac{11}{2\varepsilon_{\mathrm{IR}}}+\frac{n_f-1}{3\varepsilon_{\mathrm{IR}}}+\frac{1}{3}\ln\frac{m_t^2}{m_{\tilde{g}}^2}-\frac{8}{3}\ln(2)-\frac{25}{2}+2\pi^2+\frac{\beta_0^{(\mathrm{SQCD})}}{2}\ln\left(\frac{\mu_R^2}{M^2}\right)\\ &+n_f\left[\frac{1}{6}\ln\frac{r}{4}+\frac{9r-1}{9}c_5(r)+\frac{r-1}{2}\Big(2b_1'(r)+b_1(r)-b_4(r)\Big)\right]\Bigg\}\,f_\varepsilon(M^2)\,,\end{aligned} \tag{20a}$$

$$\begin{aligned}\mathcal{V}_{gg}^{[8_s]} \;=\;& \Bigg\{-\frac{3}{\varepsilon_{\mathrm{IR}}^2}-\frac{7}{\varepsilon_{\mathrm{IR}}}+\frac{n_f-1}{3\varepsilon_{\mathrm{IR}}}+\frac{1}{3}\ln\frac{m_t^2}{m_{\tilde{g}}^2}-\frac{8}{3}\ln(2)-\frac{19}{2}+\frac{13}{8}\pi^2+\frac{\beta_0^{(\mathrm{SQCD})}}{2}\ln\left(\frac{\mu_R^2}{M^2}\right)\\ &+n_f\left[\frac{1}{6}\ln\frac{r}{4}+\frac{9r-4}{9}c_5(r)+\frac{r-1}{2}\Big(2b_1'(r)+b_1(r)-b_4(r)\Big)\right]\Bigg\}\,f_\varepsilon(M^2)\,,\end{aligned} \tag{20b}$$

$$\begin{aligned}\mathcal{V}_{q\bar{q}}^{[8_a]} \;=\;& \Bigg\{-\frac{4}{3\varepsilon_{\mathrm{IR}}^2}-\frac{7}{2\varepsilon_{\mathrm{IR}}}-\frac{2}{3}+\frac{5}{36}\pi^2+2\ln(2)-\frac{5}{9}n_f+\frac{\beta_0^{(\mathrm{SQCD})}}{2}\ln\left(\frac{\mu_R^2}{M^2}\right)\\ &+\mathcal{A}_{q\bar{q}}^{[8_a]}(r)\Bigg\}\,f_\varepsilon(M^2)\,,\end{aligned} \tag{20c}$$

$$\begin{aligned}\mathcal{V}_{gg}^{[27_s]} \;=\;& \Bigg\{-\frac{3}{\varepsilon_{\mathrm{IR}}^2}-\frac{19}{2\varepsilon_{\mathrm{IR}}}+\frac{n_f-1}{3\varepsilon_{\mathrm{IR}}}+\frac{1}{3}\ln\frac{m_t^2}{m_{\tilde{g}}^2}-\frac{8}{3}\ln(2)-\frac{9}{2}+\pi^2+\frac{\beta_0^{(\mathrm{SQCD})}}{2}\ln\left(\frac{\mu_R^2}{M^2}\right)\\ &+n_f\left[\frac{1}{6}\ln\frac{r}{4}+\frac{r-1}{2}\Big(2c_5(r)+2b_1'(r)+b_1(r)-b_4(r)\Big)\right]\Bigg\}\,f_\varepsilon(M^2)\,,\end{aligned} \tag{20d}$$

where $m_t = 172\,\mathrm{GeV}$, $f_\varepsilon(Q^2)=(4\pi\mu^2/Q^2)^\varepsilon\,\Gamma(1+\varepsilon)$ and $\beta_0^{\mathrm{SQCD}}=3C_A-2T_Fn_f$ (with $n_f=6$) is the one-loop coefficient of the SUSY QCD beta function and the scalar functions

$b_i$, $b'_1$ and $c_5$ are defined in Appendix B. The limit $m_t \to 0$ has been taken wherever possible.

The $gg$ initiated processes into $1_s, 8_s, 27_s$ receive contributions from the diagrams depicted in Fig. 5, which do not involve squarks and from diagrams with virtual squarks depicted in Fig. 6. The latter are proportional to $n_f$, the number of quark and squark flavours. For the squarks we assume equal masses. (The general calculation for different masses for left- and righthanded squarks and for different generations is straightforward, however, the formulae are lengthy. Explicit results are presented in Ref. [60].) The $q\bar{q}$ initiated process into $8_a$ receives contributions from diagrams without and with squarks in LO already (see Fig. 2). Consequently also the corrections contain contributions from diagrams without squarks (independent of $r$) (Fig. 7) and with squarks (Fig. 8). All squark mass dependent terms are collected in the function $\mathcal{A}_{q\bar{q}}^{[8_a]}$ which is defined in Appendix B.

Born term and virtual corrections are absent for decuplet production in gluon fusion and quark-anti-quark annihilation (see Eq. (8)). The corrections from real radiation as discussed below give a (small) non-vanishing result.

The quantities $\mathcal{R}_{ij}^{[T]}$ result from the real corrections to the processes and contain the subtraction terms which originate from the renormalization of the PDFs in the $\overline{\mathrm{MS}}$ scheme. Thus the remaining infra-red divergences exactly cancel the ones present in the virtual corrections of Eq. (20). Let us start with the process $gg \to Tg$ which does not involve squarks (see Fig. 9). For the individual colour configurations we obtain

$$\begin{aligned}
\mathcal{R}_{gg}^{[1_s]}(z) &= \mathcal{R}_{gg}(z) + \frac{11z^5+11z^4+13z^3+19z^2+6z-12}{2z(1+z)^2} \\
&\quad + \frac{3}{1-z}\left[\frac{2z\,(z^3-z+2)\,(z^3-2z^2-3z-2)}{(1+z)^3}\frac{\ln(z)}{1-z} - 3\right], \qquad (21a)
\end{aligned}$$

$$\begin{aligned}
\mathcal{R}_{gg}^{[8_s]}(z) &= \mathcal{R}_{gg}(z) + 3\left\{\delta(1-z)\left(\frac{1}{2\varepsilon_{\mathrm{IR}}}+1\right) - \left[\frac{1}{1-z}\right]_+\right\} \\
&\quad + \frac{23z^5+29z^4+43z^3+43z^2+18z-12}{2z(1+z)^2} \\
&\quad + \frac{3}{1-z}\left[\frac{2z\,(z^6-2z^5-6z^4+2z^3-3z^2-4z-4)}{(1+z)^3}\frac{\ln(z)}{1-z} - 4\right], \qquad (21b)
\end{aligned}$$

$$\begin{aligned}
\mathcal{R}_{gg}^{[8_a]}(z) &= \frac{4(1-z)}{z(1-z^2)^3}\Big[(1-z^2)(21z^5+88z^4+42z^3+92z^2+17z+12) \\
&\qquad +4z(11z^5+25z^4+64z^3+12z^2+21z+3)\ln(z)\Big], \qquad (21c)
\end{aligned}$$

$$\mathcal{R}_{gg}^{[10]}(z) = \frac{80z(1-z)}{(1-z^2)^3}\Big[(1-z^2)(z^3+4z^2+z+2) + 2z^2(z^2+2z+5)\ln(z)\Big], \qquad (21d)$$

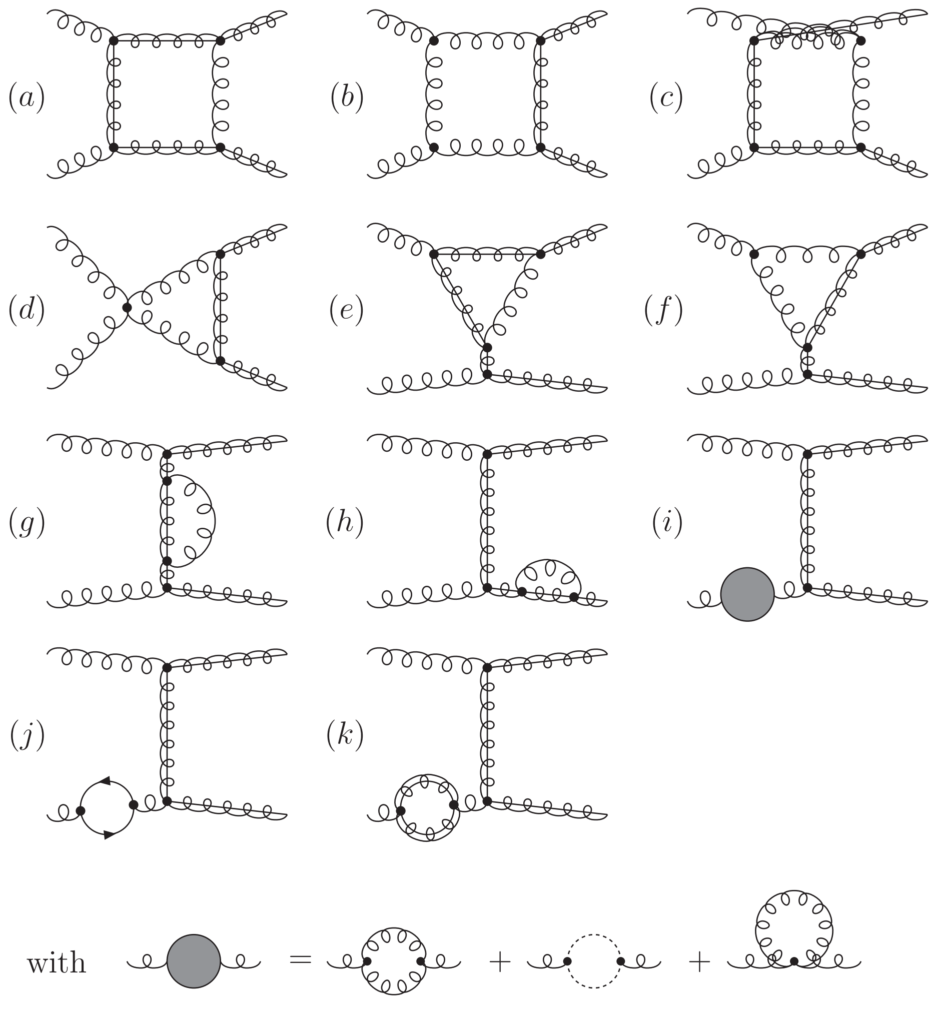


Figure 5: NLO contributions to the $gg$ initiated processes without virtual squarks (dotted lines correspond to ghost fields).

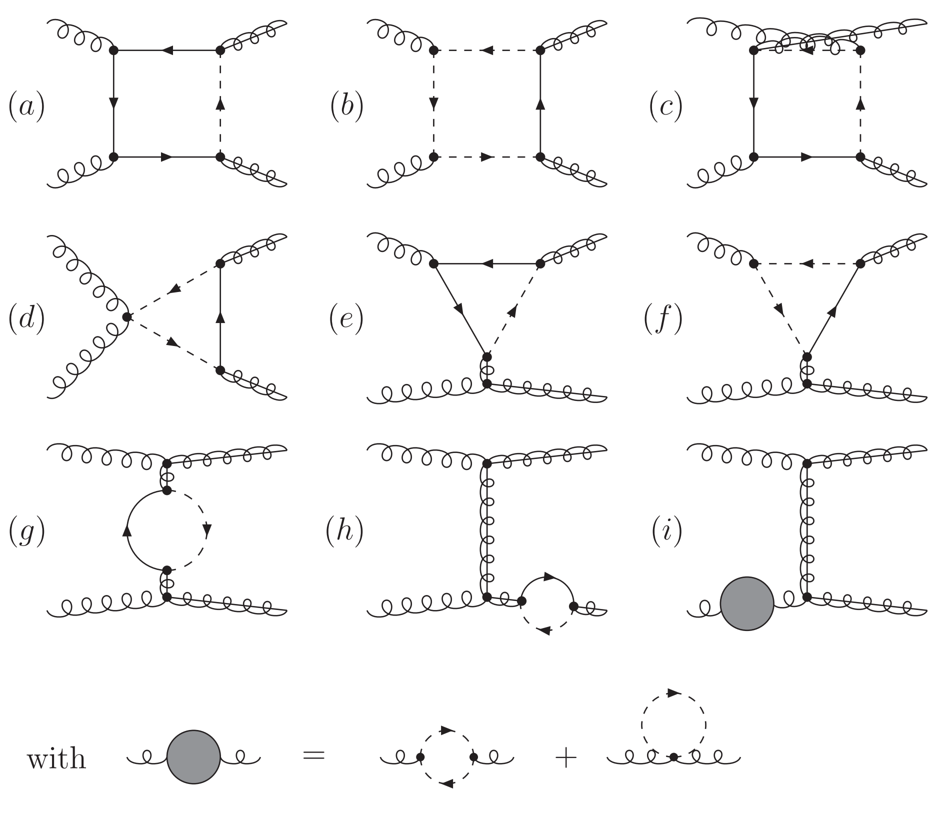


Figure 6: NLO contributions to the $gg$ initiated processes with virtual squarks (dashed lines correspond to squark fields).

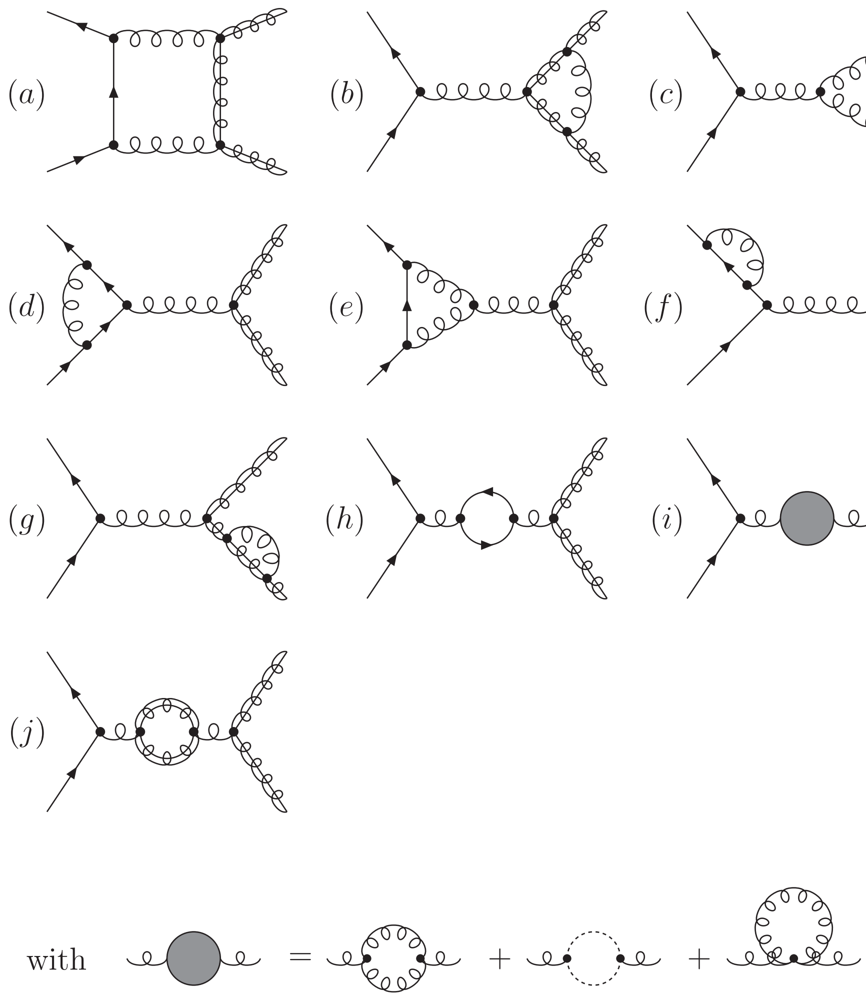


Figure 7: NLO contributions to the $q\overline{q}$ initiated processes without virtual squarks.

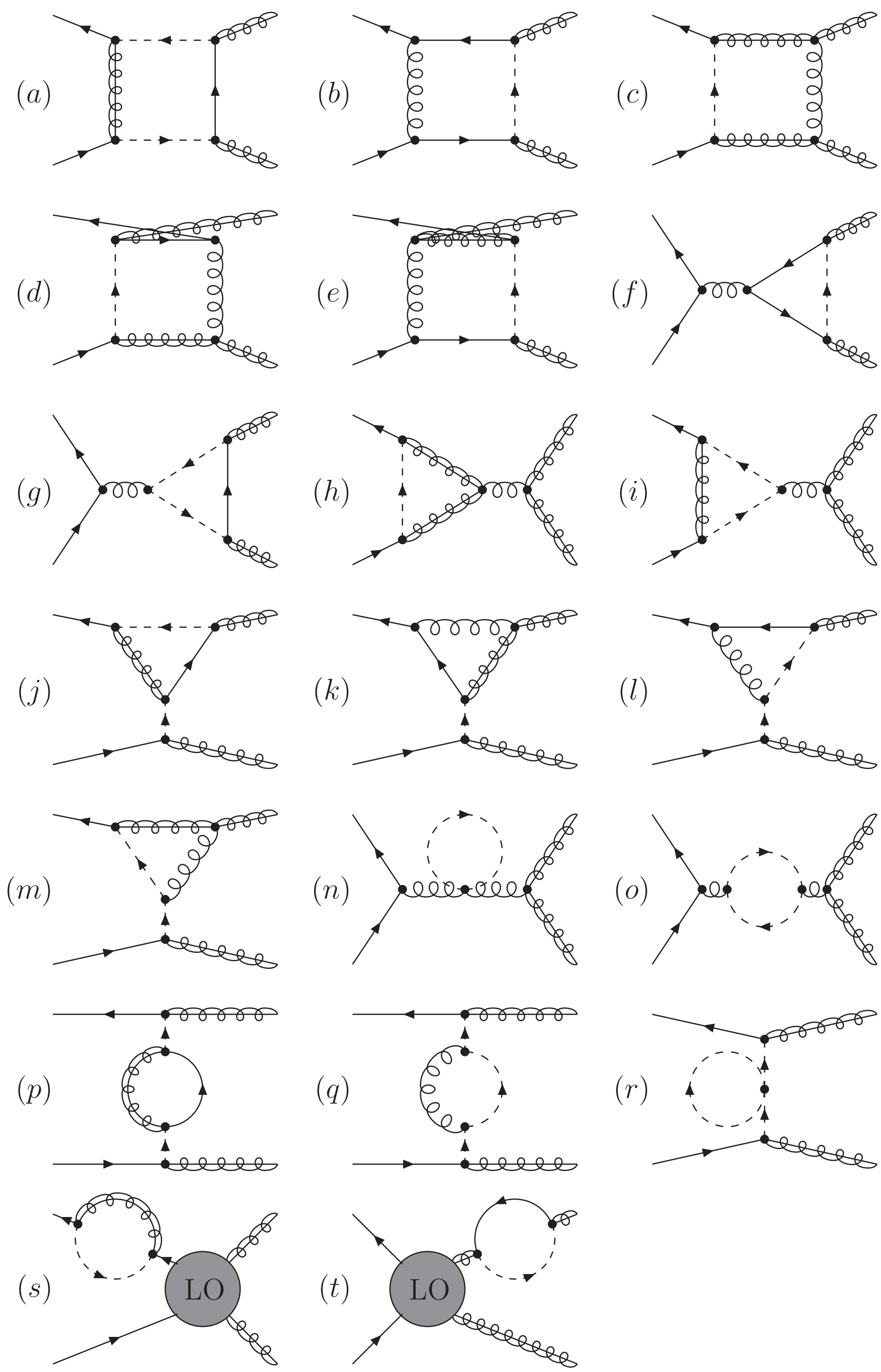


Figure 8: NLO contributions to the $q\overline{q}$ initiated processes with virtual squarks.

$$
\begin{aligned}
\mathcal{R}_{gg}^{[27_s]}(z) &= \mathcal{R}_{gg}(z) + 8\left\{\delta(1-z)\left(\frac{1}{2\varepsilon_{\mathrm{IR}}}+1\right) - \left[\frac{1}{1-z}\right]_+\right\} \\
&\quad + \frac{43z^5+59z^4+93z^3+83z^2+38z-12}{2z(1+z)^2} \\
&\quad + \frac{1}{1-z}\left[\frac{2z\left(3z^6-6z^5-28z^4+6z^3-19z^2-12z-12\right)}{(1+z)^3}\frac{\ln(z)}{1-z} - 17\right], \qquad \text{(21e)}
\end{aligned}
$$

with

$$
\begin{aligned}
\mathcal{R}_{gg}(z) &= (1-z)\mathcal{P}_{gg}(z)\left\{2\left[\frac{\ln(1-z)}{1-z}\right]_+ - \left[\frac{1}{1-z}\right]_+ \ln\left(\frac{\mu_F^2}{M^2}\right)\right\} + \left\{\frac{3}{\varepsilon_{\mathrm{IR}}^2} + \frac{11}{2\varepsilon_{\mathrm{IR}}}\right. \\
&\quad \left. - \frac{n_f-1}{3\varepsilon_{\mathrm{IR}}} - \left(\frac{11}{2} - \frac{n_f-1}{3}\right)\ln\left(\frac{\mu_F^2}{M^2}\right) - \pi^2\right\} f_\varepsilon(M^2)\,\delta(1-z)\,, \qquad (22)
\end{aligned}
$$

where $n_f = 6$. The functions $\mathcal{P}_{ij}$ are listed at the end of this Section. The conventional plus-distribution[4] is employed to regularize the singularity at $z = 1$. Note, that the cross section for the decuplet configuration (plus a gluon) is non-vanishing, albeit small.

The results for the $gq$ and $g\overline{q}$ initiated processes $gq \to Tq$ and $g\overline{q} \to T\overline{q}$ are identical and we only list the former. The corresponding function $\mathcal{R}_{gq}^{[T]}$ can be split into a term $\mathcal{H}_{gq}^{[T]}$, which originates from the diagrams depicted in Fig. 10(a)-(c), and is independent of the squark mass and a second term $\mathcal{F}_{gq}^{[T]}$ from the diagrams depicted in Fig. 10(d)-(h) and their interference with those of (a)-(c). The dependence on the factorization scale $\mu_F$ is contained in $\mathcal{H}_{gq}^{[T]}$. One finds

$$
\begin{aligned}
\mathcal{R}_{gq}^{[T]}(z) &= \mathcal{H}_{gq}^{[T]}(z) + \mathcal{F}_{gq}^{[T]}(z,r)\,, \qquad \text{(23a)} \\
\mathcal{H}_{gq}^{[T]}(z) &= \mathcal{N}_{gg}^{[T]}\left\{-\frac{1}{2}\mathcal{P}_{gq}(z)\ln\left(\frac{\mu_F^2 z}{M^2(1-z)^2}\right) - \frac{4(1-z)}{3z}\left[1-\ln(z)\right] + \frac{2z}{3}\right\}, \\
&\quad \text{for} \quad T \in \{1_s, 8_s, 27_s\}\,, \qquad \text{(23b)} \\
\mathcal{H}_{gq}^{[8_a]}(z) &= \mathcal{N}_{q\overline{q}}^{[8_a]}\left\{-\frac{1}{2}\mathcal{P}_{qg}(z)\ln\left(\frac{\mu_F^2 z}{M^2(1-z)^2}\right) + \frac{9(z+1)}{8}\ln(z)\right. \\
&\quad \left. + \frac{(1-z)(32z^2+11z+18)}{16z}\right\}, \qquad \text{(23c)} \\
\mathcal{H}_{gq}^{[10]}(z) &= 0\,, \qquad \text{(23d)}
\end{aligned}
$$

[4]The plus-distribution follows the prescription $\int_0^1 dz \left[\frac{\ln^n(1-z)}{1-z}\right]_+ f(z) \equiv \int_0^1 dz\, \frac{\ln^n(1-z)}{1-z}\left[f(z)-f(1)\right]$ for $n = 0, 1, \ldots$ and any test function $f(z)$. If the lower integration boundary is given by $1 > \rho > 0$ the plus distribution can be replaced by the $\rho$-description via $\left[\frac{\ln^n(1-z)}{1-z}\right]_+ \to \frac{\ln^{n+1}(1-\rho)}{n+1}\delta(1-z) + \left[\frac{\ln^n(1-z)}{1-z}\right]_\rho$ where the latter is defined through $\int_\rho^1 dz \left[\frac{\ln^n(1-z)}{1-z}\right]_\rho f(z) \equiv \int_\rho^1 dz\, \frac{\ln^n(1-z)}{1-z}\left[f(z)-f(1)\right]$.

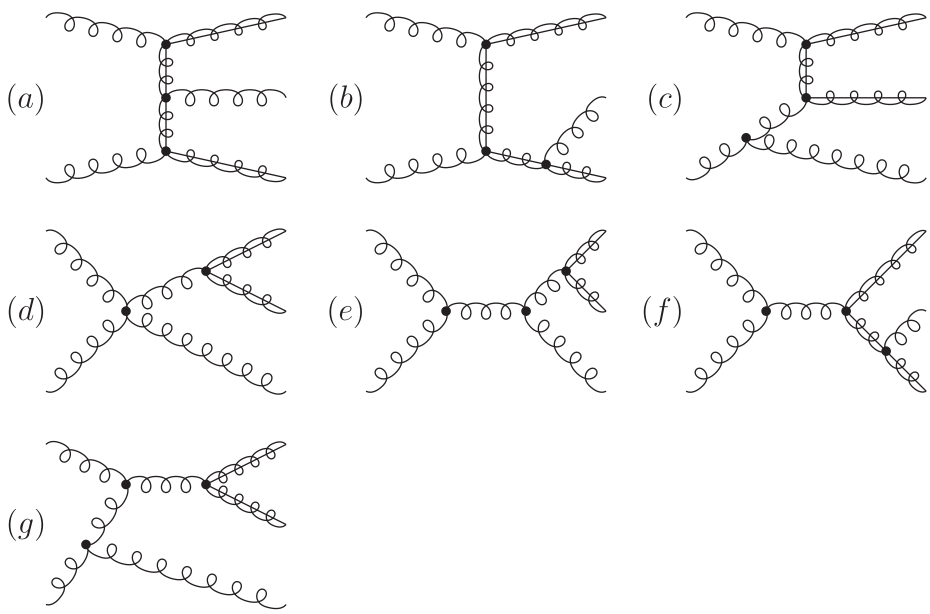


Figure 9: NLO contributions to the $gg$ initiated processes.

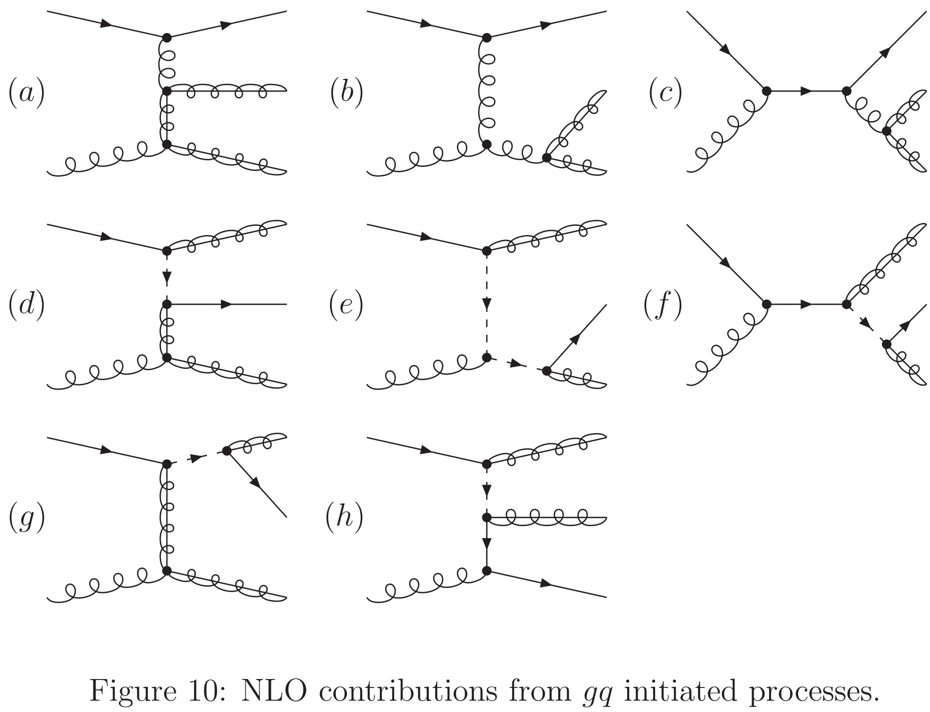


Figure 10: NLO contributions from $gq$ initiated processes.

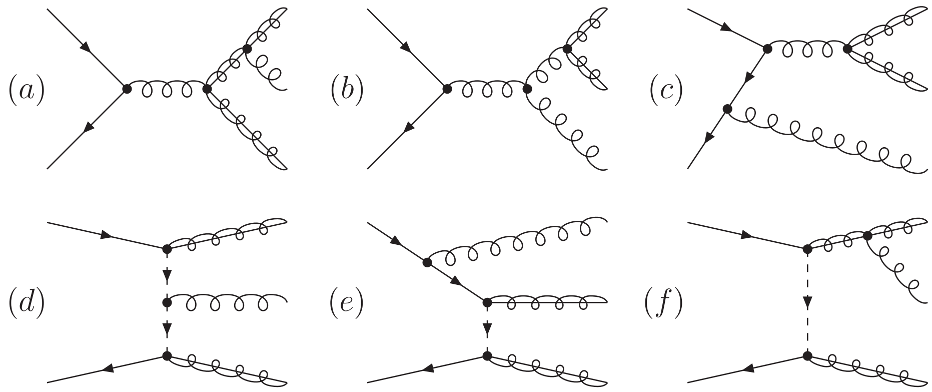

Figure 11: NLO contributions to the $q\overline{q}$ initiated processes.

and $\mathcal{H}^{[1_s]}_{gq}$ of course coincides with the result of Eq. (12) of Ref. [27]. The functions $\mathcal{F}^{[T]}_{gq}$ are listed in Appendix B, see Eqs. (32)-(36). A similar decomposition can be made for the $q\overline{q}$ initiated processes

$$
\begin{aligned}
\mathcal{R}^{[T]}_{q\overline{q}}(z) &= \mathcal{H}^{[T]}_{q\overline{q}}(z) + \mathcal{F}^{[T]}_{q\overline{q}}(z,r)\,, && \text{(24a)}\\
\mathcal{H}^{[T]}_{q\overline{q}}(z) &= \mathcal{N}^{[T]}_{gg}\frac{32}{27}z(1-z) \\
&\quad \text{for} \quad T \in \{1_s, 8_s, 27_s\}\ , && \text{(24b)}\\
\mathcal{H}^{[8_a]}_{q\overline{q}}(z) &= \left[\frac{4}{3\varepsilon^2_{\text{IR}}} + \frac{7}{2\varepsilon_{\text{IR}}} - 2\ln\left(\frac{\mu_F^2}{M^2}\right) + 3 - \frac{4\pi^2}{9}\right] f_\varepsilon(M^2)\,\delta(1-z) \\
&\quad +(1-z)\mathcal{P}_{qq}(z)\left(2\left[\frac{\ln(1-z)}{1-z}\right]_+ - \ln\left(\frac{z\mu_F^2}{M^2}\right)\left[\frac{1}{1-z}\right]_+\right) \\
&\quad +z+2-3\left[\frac{1}{1-z}\right]_+\ , && \text{(24c)}\\
\mathcal{H}^{[10]}_{q\overline{q}}(z) &= 0\,, && \text{(24d)}
\end{aligned}
$$

and $\mathcal{F}^{[T]}_{q\overline{q}}$ is again listed in Appendix B. The splitting functions entering the previous expressions are defined as

$$
\begin{aligned}
\mathcal{P}_{gg}(z) &= 6\left(\frac{1}{z} + \frac{1}{1-z} + z(1-z) - 2\right)\,, \qquad & \mathcal{P}_{gq}(z) &= \frac{4\,[1+(1-z)^2]}{3z}\,,\\
\mathcal{P}_{qg}(z) &= \frac{z^2+(1-z)^2}{2}\,, & \mathcal{P}_{qq}(z) &= \frac{8}{3}\left(\frac{1}{1-z} - \frac{1+z}{2}\right)\,. \qquad \text{(25)}
\end{aligned}
$$

# 4 Hadronic production

As described in Eq. (3), the luminosity function Eq. (4) is convoluted with the partonic cross section, which in turn is composed of the Green's function (Eq. (14)) and the short distance corrections (Eqs. (18) and (19)). For the numerical evaluation we use the PDF set MSTW2008NLO [38] which corresponds to $\alpha_s(M_Z) = 0.1202$. (Note, that for the LO study a value $\alpha_s(M_Z) = 0.1394$ was adopted.) From this value as starting point we compute $\alpha_s^{\rm SQCD}$ employing the same procedure as described before Eq. (10). We thus arrive at the cross section for proton-proton collisions, which is still differential in the mass of the gluino pair. In a first step we restrict ourselves to scenario (p) and display the region very close to threshold (Fig. 12(a)) and a wider range with $M_{\rm max} = 2000\,{\rm GeV}$ corresponding to $v^2_{\rm max} = 0.72$ (Fig. 12(b)). The contributions from the different colour configurations are shown separately. Close to threshold the strong enhancement of the singlet is contrasted with the strong suppression of the twenty-seven representation. For larger $M$ and correspondingly larger relative velocities the final state interaction becomes less relevant and about 200 GeV above threshold the twenty-seven representation starts to dominate. (This behaviour is quite similar to the one of top pair production with dominant singlet close to and dominant octet far above threshold.). The process $q\overline{q} \to [8_a]$ is non-vanishing in Born approximation. However, for squark and gluino masses being roughly equal it is strongly suppressed. This suppression is also present at NLO. The contribution from the decuplet, which is absent in Born approximation, remains small throughout. In Fig. 13 we compare this result (solid curve) with the NLO result using a fixed order treatment for the Green's function, i.e. we replace the imaginary part of the Green's function by its expansion in $\alpha_s$, first keeping $\Gamma_{\tilde{g}}$ non-vanishing (dotted curve) and then in the limit $\Gamma_{\tilde{g}} \to 0$ (dashed curve)

$$\mathrm{Im}\, G^{[R]} \quad \to \quad \frac{m_{\tilde{g}}^2}{4\pi}\, v\, \left(1 + C^{[R]}\frac{\alpha_s \pi}{2v}\right)\,, \tag{26}$$

leaving hard correction and PDFs unchanged. In the threshold region the latter choice is a valid approximation to the complete fixed order NLO prediction for the cross section. For invariant masses above 1700 GeV fixed order and Green's function modulated approach agree reasonably well, between threshold and 1600 GeV they differ significantly. (Inclusion of finite width effects is quite irrelevant in the fixed order treatment.) The integrated difference between dashed and solid curves amounts to 0.183 pb and is a measure of the threshold enhancement, that would escape the strict fixed order treatment. Relative to the total cross section[5] for hadro-production of two gluinos, which, within scenario (p), amounts to $\sigma_{\rm tot} = 2.59\,{\rm pb}$, this corresponds to an enhancement of 7.1%.

The renormalization ($\mu_R$) and factorization ($\mu_F$) scale dependence of the differential cross section is shown in Fig. 14 for three different choices, namely $\mu_R = \mu_F = m_{\tilde{g}}, 2m_{\tilde{g}}, 4m_{\tilde{g}}$ and again for the two regions in $M$ and for the LO and the NLO prediction. Note, that we keep the Green's function unchanged and identify factorization and renormalization

[5]This result has been obtained with the code `Prospino2` [5] in NLO, using CTEQ5 PDFs.

(a)

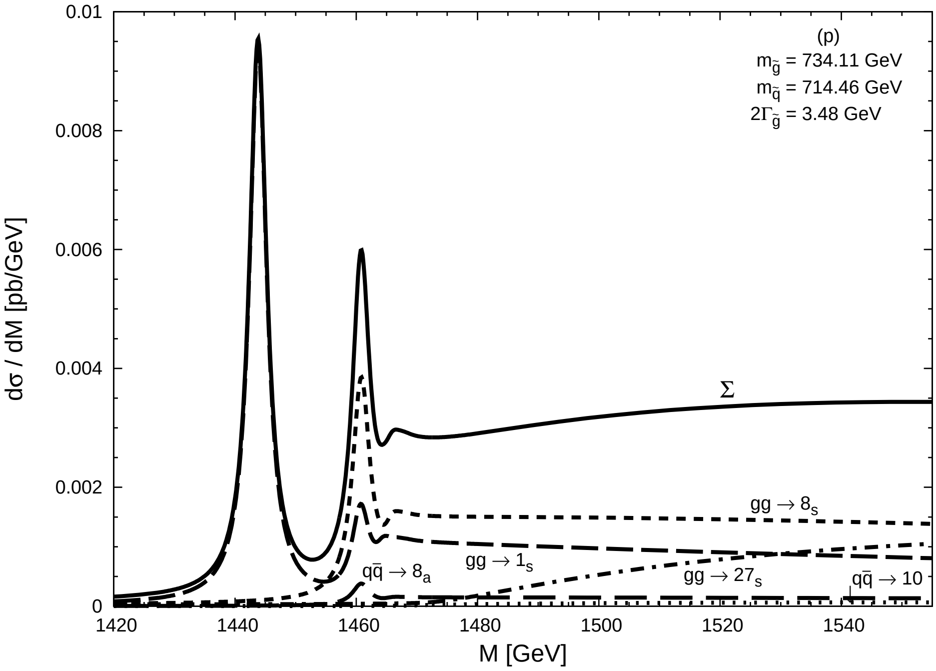


(b)

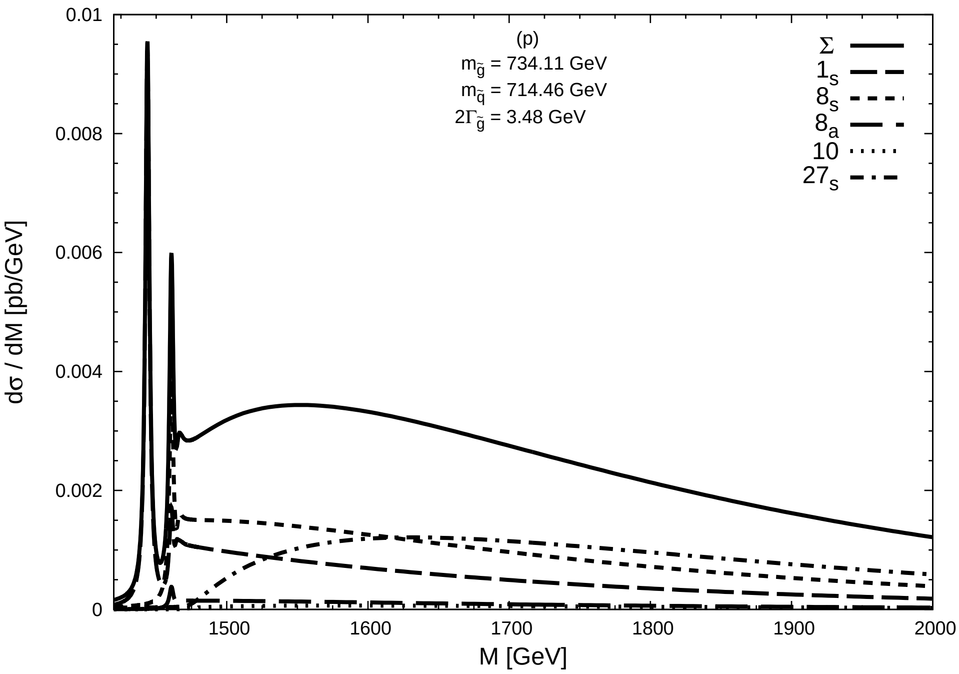


Figure 12: NLO prediction for the differential cross section for scenario (p) for two different regions of $M$.

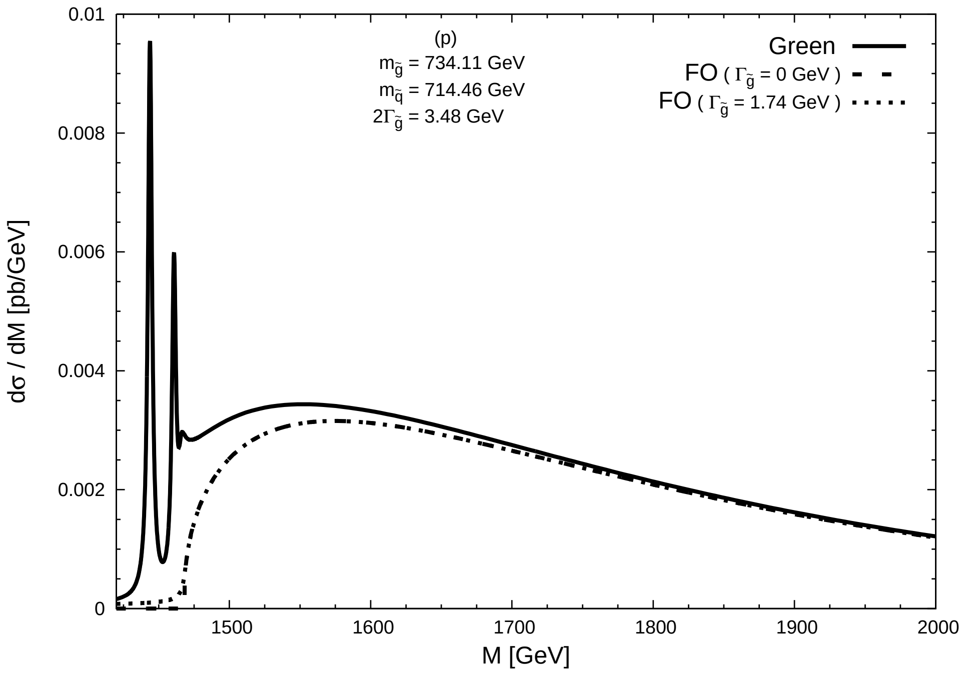


Figure 13: Prediction for the differential cross section in NLO using the Green's function, in comparison with the fixed order cross section without and with vanishing single decay width for scenario (p).

(a)

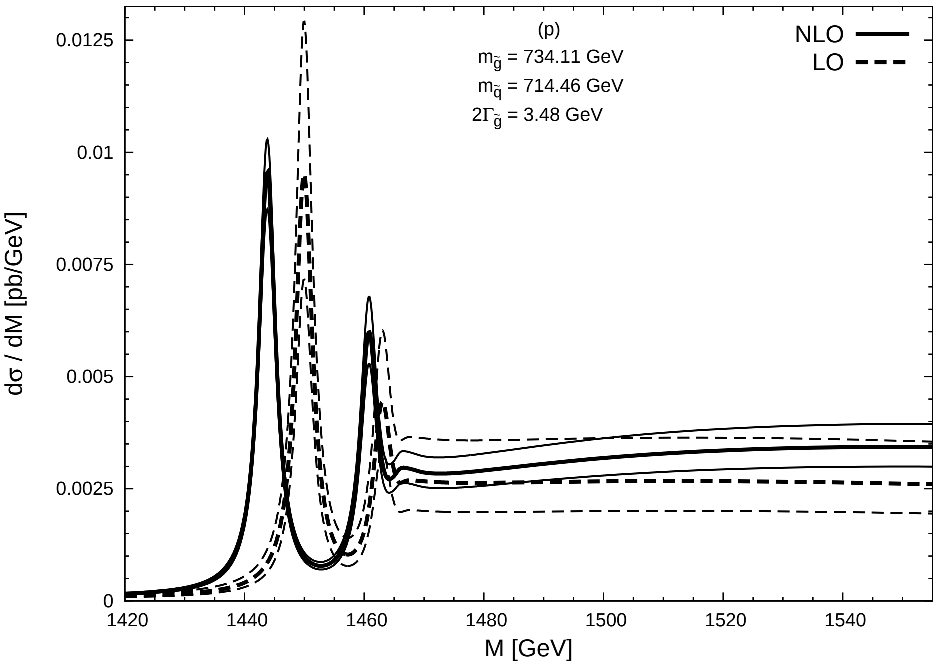


(b)

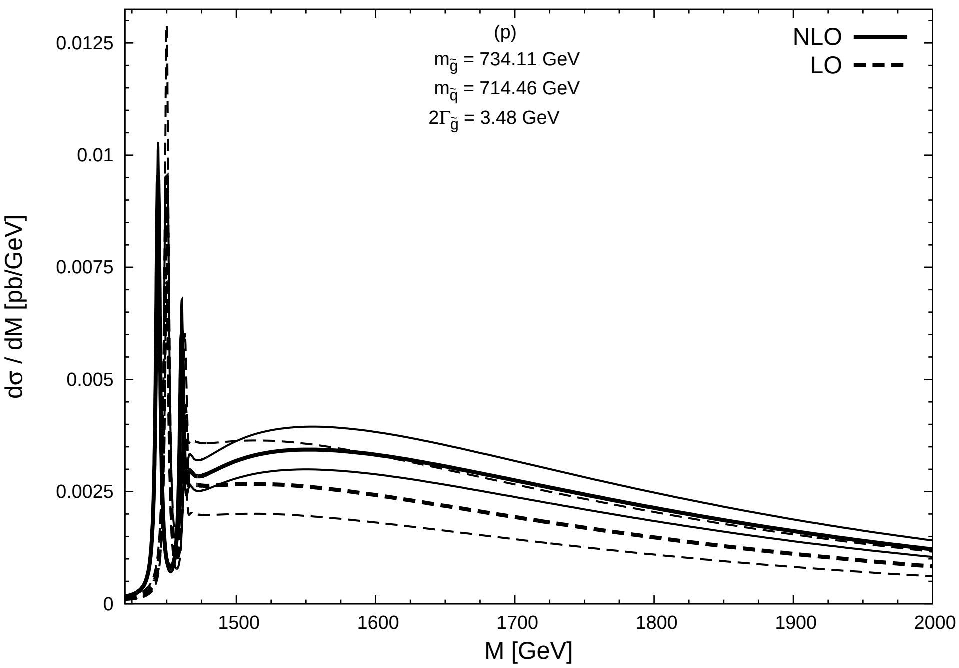


Figure 14: Renormalization- and factorization-scale dependence of the differential cross section for scenario (p) for two different regions of $M$.

| | $\alpha_s(2m_{\tilde{g}})$ | $1_s$ | $8_s$ | $8_a$ | 10 | $27_s$ |
|---|---|---|---|---|---|---|
| | NLO calculation | | | | | |
| $s^{\rm LO}$ [fb/GeV$^2$] | 0.1031 | 5.00 | 10.0 | 0.137 | – | 15.0 |
| $s^{\rm NLO}$ [fb/GeV$^2$] | 0.0923 | 4.98 | 13.3 | 1.40 | 0.984 | 29.5 |
| $s^{\rm NLO}/s^{\rm LO} - 1$ [%] | – | −0.4 | 33 | 922 | – | 96.7 |
| | approximation | | | | | |
| $s^{\rm LO}$ [fb/GeV$^2$] | 0.0954 | 4.29 | 8.57 | 0.117 | – | 12.9 |
| $s^{\rm NLO}$ [fb/GeV$^2$] | 0.0862 | 6.50 | 14.0 | 0.136 | – | 23.5 |
| $s^{\rm NLO}/s^{\rm LO} - 1$ [%] | – | 51.5 | 63.4 | 16.2 | – | 82.2 |

Table 4: Comparison of full and approximate NLO results (see text).

scales. For the LO prediction we use the parameters described at the end of Section 2. Between LO and NLO we observe a slight shift of the location of the resonance peaks by about 10 GeV, a slight increase of the cross section by about 15% and a reduction of the scale dependence. For the NLO prediction this residual $\mu$ dependence amounts to 15%.

In Figs. 15 and 16 the corresponding results are shown for scenarios (a) and (q). The gluino masses of (p), (a) and (q) are comparable, the difference between gluino and squark mass, however, increases and, correspondingly, the gluino decay rate. For scenario (a) with $\Delta M = 13.89$ GeV and $2\Gamma_{\tilde{g}} = 9.08$ GeV the $1S$ peak is still clearly visible, for scenario (q), with $\Delta M = 15.79$ GeV and $2\Gamma_{\tilde{g}} = 22.92$ GeV, the resonant structures have essentially disappeared. Nevertheless, final state interaction leads to a significantly enhanced cross section in the threshold region also in these two cases (Fig. 17(a) and (b)).

The results for the invariant mass distribution with $\sqrt{s} = 7$ TeV are shown in Fig. 18(a) and (b), restricting ourselves again to scenario (p). These results are qualitatively similar to those of Fig. 12. A reduction of the cross section by a factor 20 is observed.

In Tab. 4 we investigate the relative size of the corrections for the different states and contrast our result with those based on an approximation discussed in [30]. The latter employs a hard correction factor, which is different for quark-anti-quark annihilation and gluon fusion, does not distinguish between different colour representations and has been numerically extracted from the continuum result [5]. Furthermore, it includes the logarithmically enhanced terms from soft radiation, which are determined by the colour charge of initial and final states. To allow for a consistent comparison, we employ for both cases MSTW2008LO PDFs with $\alpha_s(M_Z) = 0.1394$ in LO and MSTW2008NLO PDFs with $\alpha_s(M_Z) = 0.1202$ for the (approximate) NLO result. However, following [30] we use for the approximate treatment two loop running with $n_f = 5$ both for LO and NLO. The corresponding $\alpha_s$ values are listed in the table. In Tab. 4 we also show the results for the quantities $s^{\rm LO}$ and $s^{\rm NLO}$ which were obtained from the corresponding results for $\mathrm{d}\sigma/\mathrm{d}M$

(a)

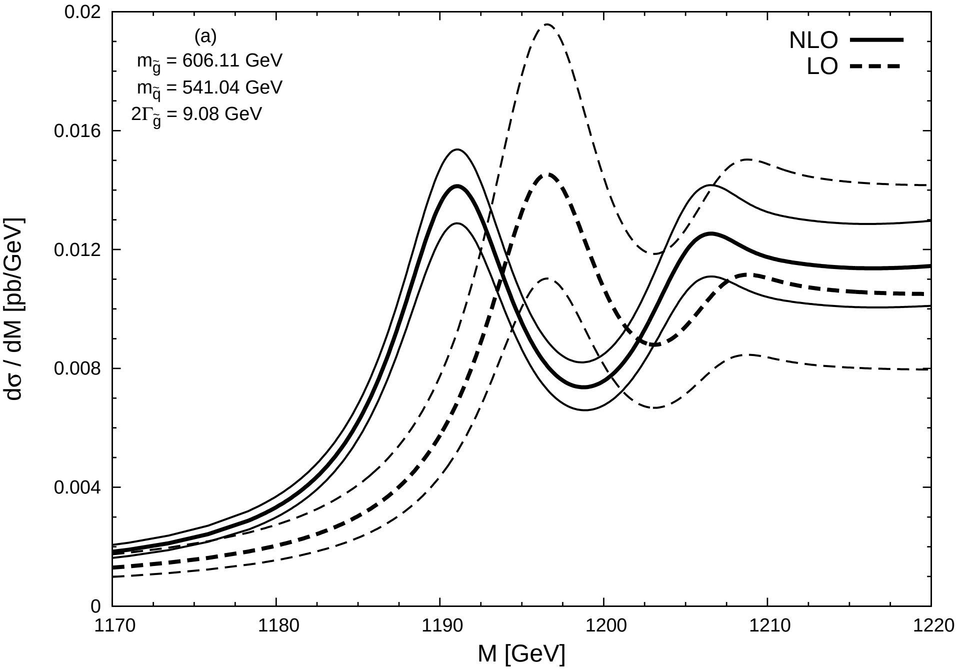


(b)

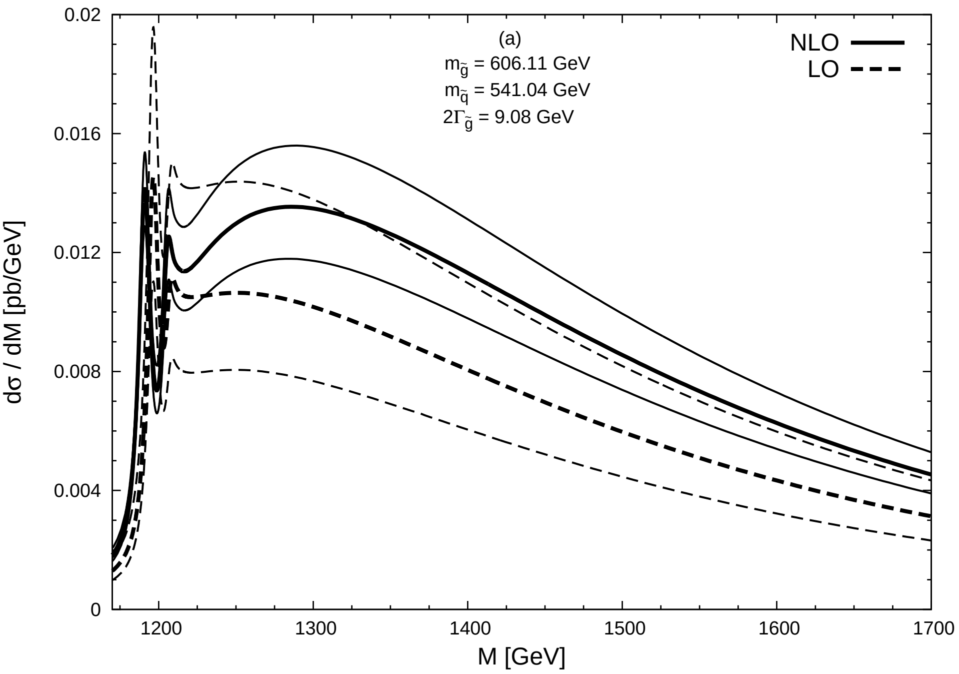


Figure 15: Renormalization- and factorization-scale dependence of the differential cross section of scenario (a) for two different regions of $M$.

(a)

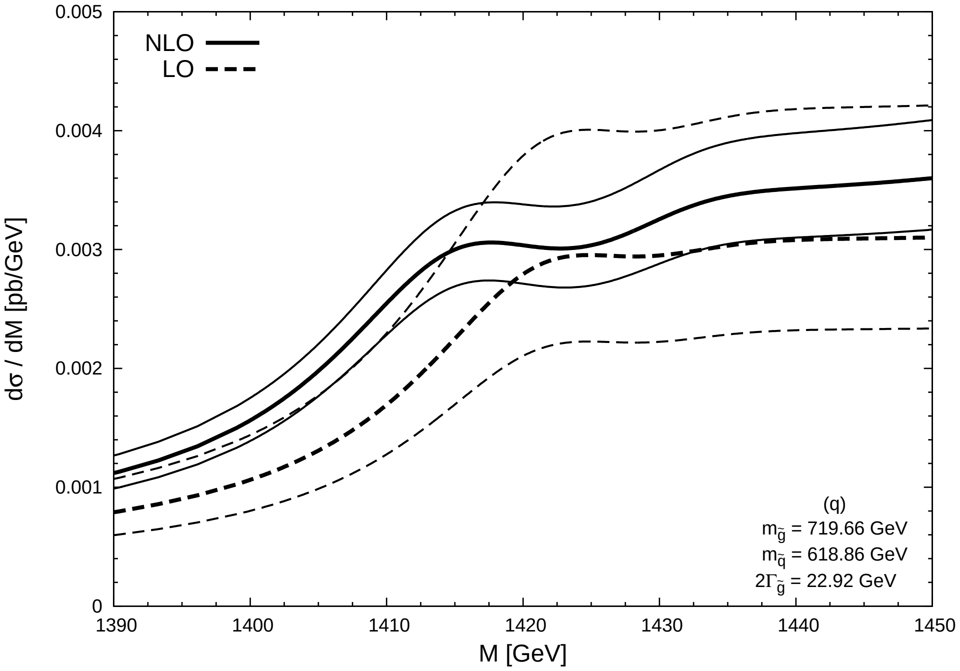


(b)

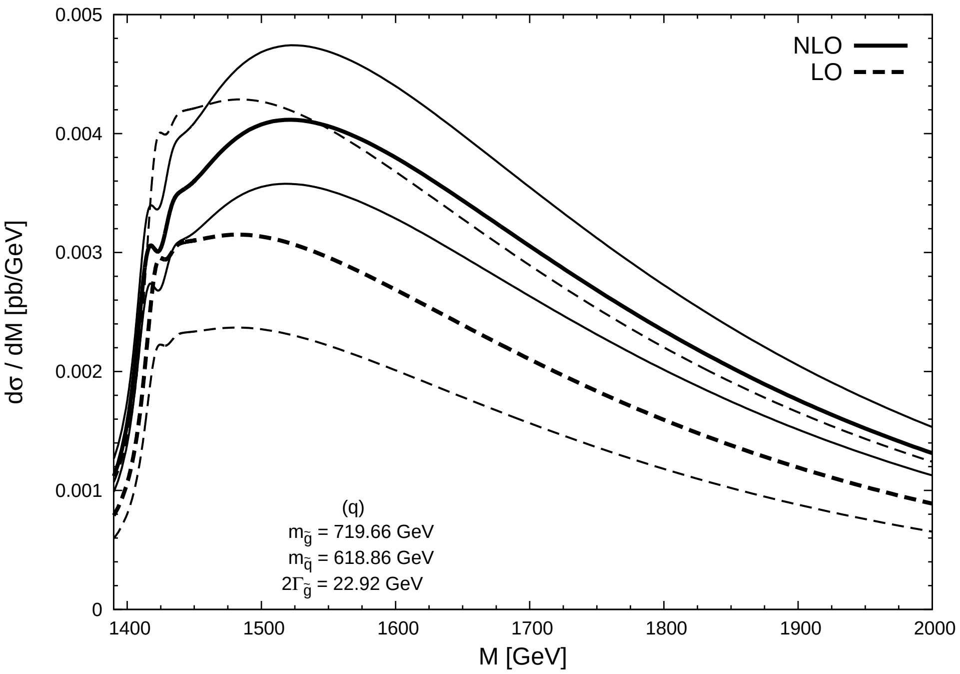


Figure 16: Renormalization- and factorization-scale dependence of the differential cross sections of scenario (q) for two different regions of $M$.

(a)

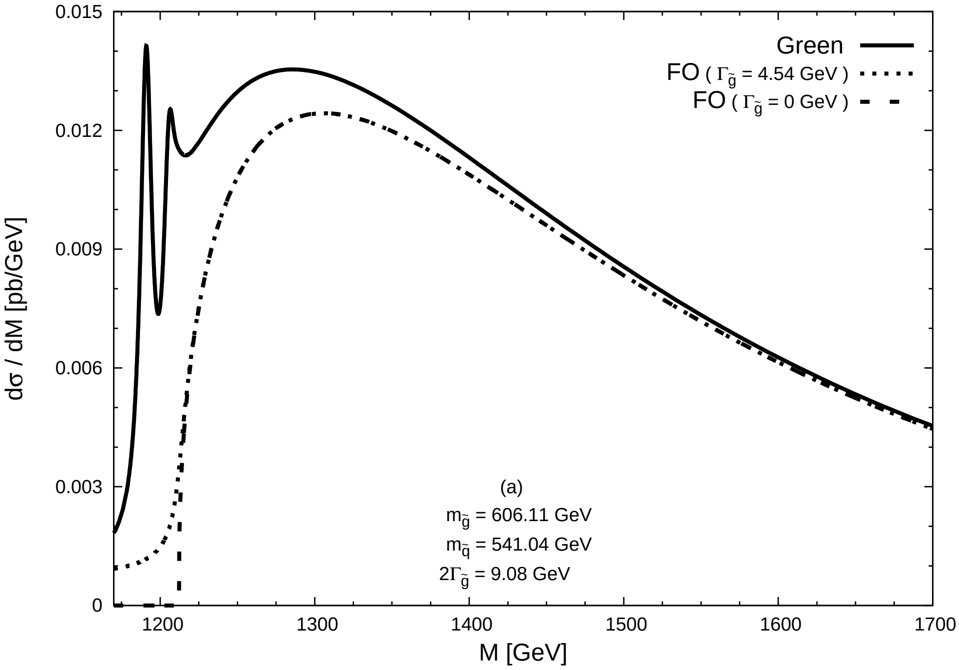


(b)

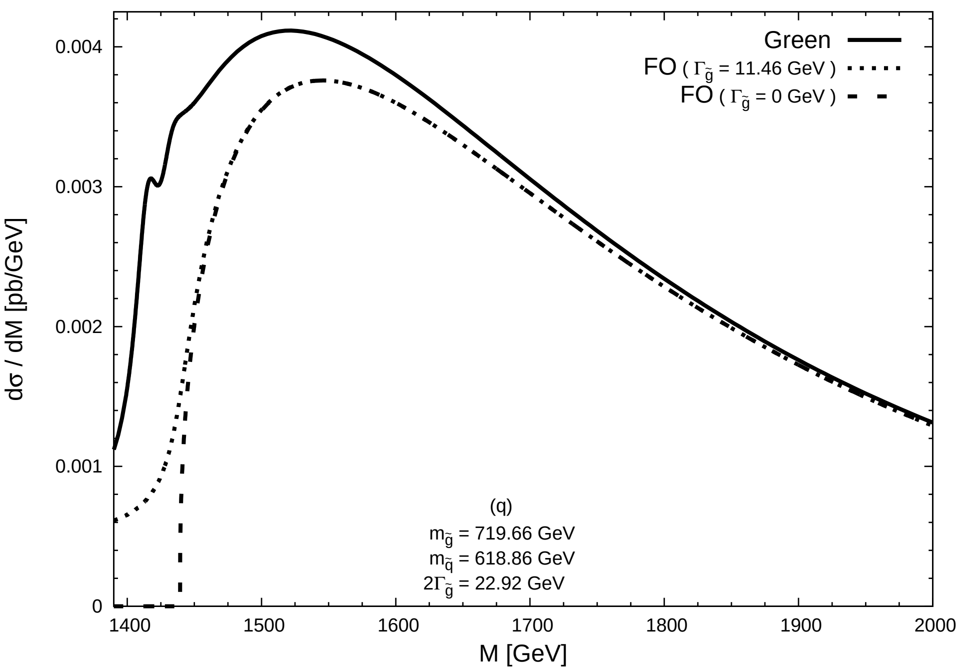


Figure 17: Prediction for the differential cross section in NLO using the Green's function in comparison with the fixed order cross section without and with vanishing single decay width for scenarios (a) and (q).

(a)

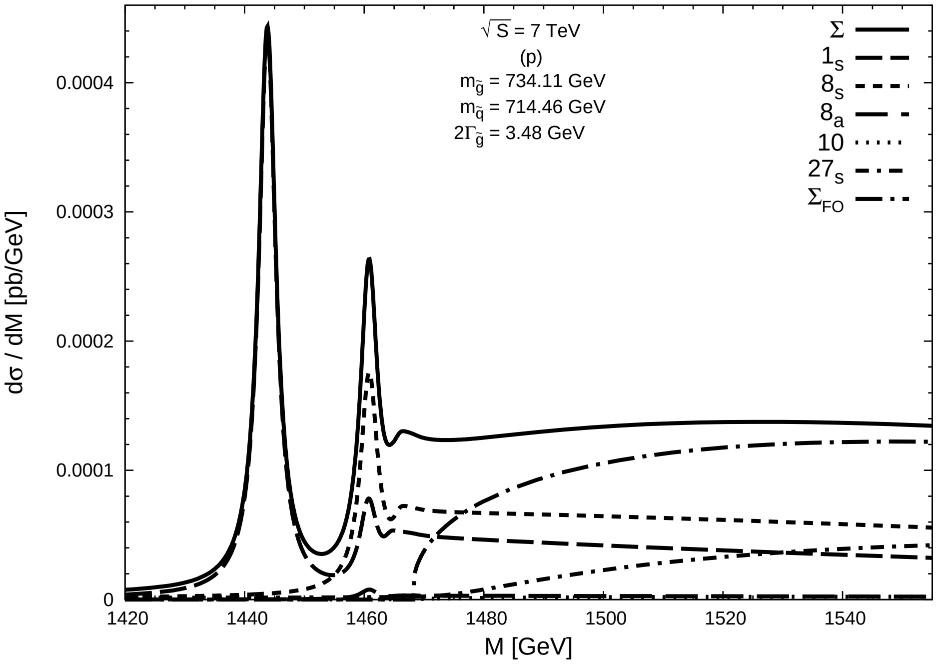


(b)

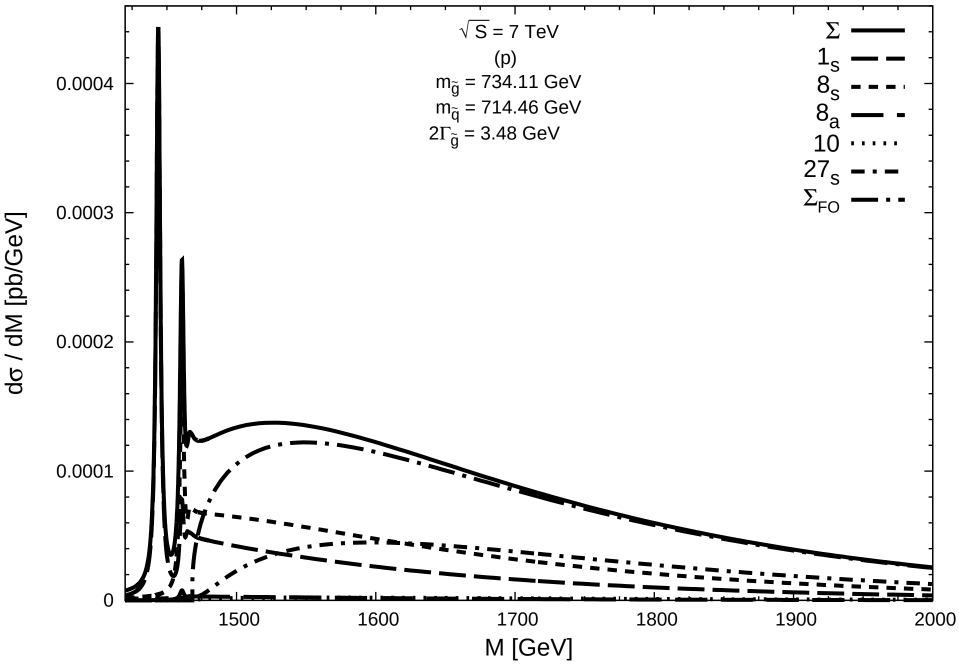


Figure 18: NLO prediction for the differential cross section at $\sqrt{s} = 7\,\mathrm{TeV}$ for scenario (p) and comparison to the fixed order cross section with vanishing single decay width.

with $G \equiv m_{\tilde{g}}^2/(4\pi)$. In this way we remove the dependence on the Green's function. The hard corrections are only weakly dependent on $M$ and we adopt $M = 2m_{\tilde{g}}$ as reference point. Furthermore, we adopt benchmark point (a), corresponding to $m_{\tilde{g}} = 606.11\,\text{GeV}$ and $m_{\tilde{q}} = 541.04\,\text{GeV}$.

The difference between the two LO results can be traced to the different values of $\alpha_s$. The difference between the relative size of the corrections is due to additional subprocesses present in the full calculation and the appearance of additional contributions with virtual squarks.

# 5 Conclusions

The next-to-leading order analysis for hadronic production of gluino pairs close to threshold has been presented. The matching coefficients were evaluated separately for the different colour configurations of gluino pairs with relative angular momentum zero. The cross section is strongly affected by final state interaction which is encoded in the NLO Green's function and which depends on the gluino decay rate, the colour configuration and the invariant mass of the pair. We have investigated three different SUSY-scenarios covering a wide range of gluino and squark masses, and studied the renormalization and factorization scale dependence of the result. Compared to the leading order prediction the result is more stable, and, for $\mu$ between $m_{\tilde{g}}$ and $4m_{\tilde{g}}$, varies by $\pm 15\%$. The complete NLO threshold production of $(\tilde{g}\tilde{g})$ boundstates considered in this paper enhances the fixed order prediction by typically 7% to 9%.

# A The Generalized Hypergeometric Function

The Generalized Hypergeometric Function (GHF) is defined by the series

$$ {}_pF_q(a_1, a_2, \ldots, a_p; b_1, \ldots, b_q; z) \;=\; \sum_{n=0}^{\infty} \frac{(a_1)_n (a_2)_n \cdots (a_p)_n}{(b_1)_n \cdots (b_q)_n} \frac{z^n}{n!}\,, \tag{27} $$

with the Pochhammer symbols $(x)_n = \Gamma(x+n)/\Gamma(x)$ and the restriction $b_i \neq 0, -1, \ldots$ for $i = 1, 2, \ldots, q$. The series converges if one of the following conditions holds

(1) $p \leq q,\ |z| < \infty\,,$

(2) $p = q+1,\ |z| < 1\,,$

(3) $p = q+1,\ |z| = 1,\ \mathrm{Re}\left(\sum_{n=1}^{q} b_n - \sum_{n=1}^{q+1} a_n\right) > 0\,,$

(4) $p = q+1,\ |z| = 1,\ z \neq 1,\ -1 < \mathrm{Re}\left(\sum_{n=1}^{q} b_n - \sum_{n=1}^{q+1} a_n\right) \leq 0\,.$

For the numerical evaluation of the Green's function of Eq. (14) it is necessary to evaluate the GHF ${}_4F_3(1,1,1,1;2,2,x;1)$ for $x \in \mathbb{C}$, hence the remaining arguments have to fulfill condition (3). For $\mathrm{Re}(x) < 0$ the convergence of the series is not guarantied.

In Ref. [61] the following algorithm is introduced which allows to decompose this function via partial fractioning in GHFs with convergent series representation. Following Ref. [61] we employ the following identity

$$
\begin{aligned}
{}_4F_3(1,1,1,1;2,2,x;1) \quad = \quad & \frac{1}{4x^2(2-x)^2}\Big[\, 4(x-1)^4\, {}_4F_3(1,1,1,1;2,2,x+1;1) \\
& +2x(7-4x)\, {}_4F_3(1,1,1,1;3,2,x;1) \\
& +x(x-2)\, {}_4F_3(1,1,1,1;3,3,x;1)\Big] . \qquad (28)
\end{aligned}
$$

For arbitrary values $\mathrm{Re}(x) < 0$ with $x \neq -1, -2, \ldots$ this relation is applied repeatedly, leading to the following results

$$
\begin{aligned}
{}_4F_3(1,1,1,1;a,a,x;1) \quad = \quad & \frac{1}{a^2 x\big(x-2(2-a)\big)(a-x)^2} \\
& \times\Big[\, a^2(x-1)^4\, {}_4F_3(1,1,1,1;a,a,x+1;1) \\
& \quad +a(a-1)^3 x(3a+1-4x)\, {}_4F_3(1,1,1,1;a+1,a,x;1) \\
& \quad +(a-1)^4 x(x-a)\, {}_4F_3(1,1,1,1;a+1,a+1,x;1)\Big] , \\
{}_4F_3(1,1,1,1;a,b,x;1) \quad = \quad & \frac{1}{a+b+x-4}\Big[\frac{(a-1)^4}{a(a-b)(a-x)}\, {}_4F_3(1,1,1,1;a+1,b,x;1) \\
& +\frac{(b-1)^4}{b(b-a)(b-x)}\, {}_4F_3(1,1,1,1;a,b+1,x;1) \\
& +\frac{(x-1)^4}{x(x-a)(x-b)}\, {}_4F_3(1,1,1,1;a,b,x+1;1)\Big] ,
\end{aligned}
\qquad (29)
$$

with $a, b \in \mathbb{N}\backslash\{0,1\}$ and $a \neq b$.

# B Corrections from virtual and real emission

The missing piece for the virtual corrections to the hard part of the partonic cross section for the $[8_a]$ configuration (see Eq.(20)) is

$$
\begin{aligned}
\mathcal{A}_{q\bar{q}\to 8_a}(r) \;=\;& \frac{3a_1(r)}{4(r-1)} - \frac{(r^2-5)b_1(r)}{12(r-1)^2} + \frac{(r-3)(r+1)^2 b_2(r)}{24(r-1)^2} + \frac{(4r-13)b_3(r)}{12} \\
& - \frac{2(r^2-2r+5)b_4(r)}{3(r^2-1)} - \frac{16 r b_5(r)}{3(r^2-1)} + \frac{8b_6(r)}{3(r+1)} + \frac{2(r-1)b_2'(r)}{3} \\
& - \frac{(r+1)^2(r^2-2r+5)c_1(r)}{24(r-1)^2} - \frac{(r^3-5r^2+11r-15)c_2(r)}{12(r-1)^2} \\
& - \frac{3(r+1)(r^2-6r+17)c_3(r)}{8(r-1)} - \frac{3(r+1)(r^2-2r+5)c_4(r)}{4(r-1)} \\
& - \frac{(3r^2-4r-17)\ln(2)}{4(r-1)} - \frac{18r^3+14r^2+23r-101}{12(r^2-1)} \\
& + n_f \left[ \frac{(r-5)a_1(r)}{6(r-1)} - \frac{r b_1(r)}{3} + \frac{(r+1)^2 b_2(r)}{6(r-1)} \right. \\
& \qquad \left. + (r-1)b_1'(r) + \frac{3r^2+r+2}{18(r-1)} \right], \qquad (30)
\end{aligned}
$$

where the scalar one-, two- and three-point functions are

$$
\begin{aligned}
A_0(m_{\tilde{q}}^2) &= m_{\tilde{q}}^2\,\Delta + m_{\tilde{g}}^2\,a_1(r)\ , \\
\mathrm{Re}\left\{B_0(m_{\tilde{g}}^2; m_{\tilde{q}}^2, 0)\right\} &= \Delta + b_1(r)\ , \\
\mathrm{Re}\left\{B_0(4m_{\tilde{g}}^2; m_{\tilde{q}}^2, m_{\tilde{q}}^2)\right\} &= \Delta + b_2(r)\ , \\
B_0(0; m_{\tilde{q}}^2, m_{\tilde{g}}^2) &= \Delta + b_3(r)\ , \\
B_0(-m_{\tilde{g}}^2; m_{\tilde{q}}^2, 0) &= \Delta + b_4(r)\ , \\
B_0(m_{\tilde{q}}^2; m_{\tilde{q}}^2, 0) &= \Delta + b_5(r)\ , \\
\mathrm{Re}\left\{B_0(m_{\tilde{q}}^2; m_{\tilde{g}}^2, 0)\right\} &= \Delta + b_6(r)\ , \\
m_{\tilde{g}}^2\,\mathrm{Re}\left\{B_0'(m_{\tilde{g}}^2; m_{\tilde{q}}^2, 0)\right\} &= b_1'(r)\ , \\
m_{\tilde{g}}^2 B_0'(0\,; m_{\tilde{g}}^2, m_{\tilde{q}}^2) &= b_2'(r)\ , \\
m_{\tilde{g}}^2\,\mathrm{Re}\left\{C_0(4m_{\tilde{g}}^2, 0, 0\,; m_{\tilde{q}}^2, m_{\tilde{q}}^2, m_{\tilde{g}}^2)\right\} &= c_1(r)\ , \\
m_{\tilde{g}}^2\,\mathrm{Re}\left\{C_0(0, -m_{\tilde{g}}^2, m_{\tilde{g}}^2; m_{\tilde{g}}^2, m_{\tilde{g}}^2, 0)\right\} &= c_2(r)\ , \\
m_{\tilde{g}}^2 C_0(0, -m_{\tilde{g}}^2, m_{\tilde{g}}^2; m_{\tilde{g}}^2, m_{\tilde{q}}^2, 0) &= m_{\tilde{g}}^2 C_0(4m_{\tilde{g}}^2, 0, 0\,; m_{\tilde{g}}^2, m_{\tilde{g}}^2, m_{\tilde{q}}^2) \;=\; c_3(r)\ , \\
c_4(r) &= -\frac{1}{r+1}\left[1 + \ln\left(\frac{r+1}{2}\right) - \frac{r}{r+1}\ln(r)\right], \\
m_{\tilde{g}}^2\,\mathrm{Re}\left\{C_0(0, -m_{\tilde{g}}^2, m_{\tilde{g}}^2; m_{\tilde{q}}^2, m_{\tilde{g}}^2, 0)\right\} &= c_5(r)\,, \qquad (31)
\end{aligned}
$$

with the conventions of [62] and $\Delta = 1/\varepsilon_{\mathrm{UV}} - \gamma_E + \ln[4\pi\mu_R^2/(2m_{\tilde{g}})^2]$. The remaining functions complete the real corrections

$$
\begin{aligned}
\mathcal{F}_{gq}^{[1_s]}(z,r) &= \Big[9r(r+1)^3z^4-(r-1)(r+1)^2z^3-2(r+1)(19r+35)z^2 \\
&\quad -32(r+1)z-64\Big]\frac{16z}{27\left[(r+1)z-2\right]^2\left[(r+1)z+2\right]^3}\ln(z) \\
&+\Big[(r+1)^3(21r+5)z^4+2(r+1)^2(5r+9)z^3+4(r+1)(23r-29)z^2 \\
&\quad +200(r+1)z-224\Big]\frac{2z\left[5z(r+1)-8\right]\ln\left(1+2\frac{1-z}{z(r+1)}\right)}{243\left[(r+1)z-2\right]^2\left[(r+1)z+2\right]^3} \\
&+\Big[(r+1)^3(57r+41)z^4+4(r+1)^2(81r^2+61r-36)z^3 \\
&\quad -4(r+1)(55r+71)z^2-16(r+1)(81r+133)z+256\Big] \\
&\quad \times\frac{4(1-z)}{243(r+1)\left[z^2(r+1)^2-4\right]^2}\,,
\end{aligned}
\tag{32}
$$

$$
\begin{aligned}
\mathcal{F}_{gq}^{[8_s]}(z,r) &= \Big[9r(r+1)^3z^4-4(r-1)(r+1)^2z^3-4(r+1)(11r+26)z^2 \\
&\quad -40(r+1)z-80\Big]\frac{32z\ln(z)}{27\left[(r+1)z-2\right]^2\left[(r+1)z+2\right]^3} \\
&+\Big[(r+1)^4(33r+28)z^5-4(r+1)^3(37r-14)z^4 \\
&\quad +4(r+1)^2(47r-175)z^3+8(r+1)(33r+163)z^2 \\
&\quad -16(86r+131)z+1120\Big]\frac{8z\ln\left(1+2\frac{1-z}{z(r+1)}\right)}{243\left[(r+1)z-2\right]^2\left[(r+1)z+2\right]^3} \\
&+\Big[(r+1)^3(24r+19)z^4+(r+1)^2(81r^2+56r-45)z^3 \\
&\quad -4(r+1)(11r+16)z^2-4(r+1)(81r+191)z+80\Big] \\
&\quad \times\frac{32(1-z)}{243(r+1)\left[z^2(r+1)^2-4\right]^2}\,,
\end{aligned}
\tag{33}
$$

$$
\begin{aligned}
\mathcal{F}_{gq}^{[8_a]}(z,r) \;=\; & \Big[ 9(r-1)^2(r+1)^4 z^6 + (r+1)^3(67r^2-186r+67)z^5 \\
& -(r+1)^2(13r^3+207r^2-81r-67)z^4 \\
& -2(r+1)^2(85r^2+100r-233)z^3 - 36(r+1)(5r^2-6r-3)z^2 \\
& +72(7r^2+18r+3)z+576r \Big] \frac{32\ln(z)}{27(r+1)^2\left[(r+1)z-2\right]^2\left[(r+1)z+2\right]^3} \\
& -\Big[ (r+1)^4(3r^3+35r^2+13r+13)z^6 \\
& -2(r+1)^3(35r^3-195r^2+353r-57)z^5 \\
& -8(r+1)^2(5r^3+125r^2-189r+91)z^4 \\
& +16(r+1)(15r^3+7r^2+25r+97)z^3 \\
& +16(19r^3+11r^2-227r-91)z^2 + 32(r^2+82r+17)z - 1024r \Big] \\
& \times \frac{4\ln\left(1+2\frac{1-z}{z(r+1)}\right)}{27(r+1)^2\left[(r+1)z-2\right]^2\left[(r+1)z+2\right]^3} \\
& +\Big[ (r-1)(r+1)^3(21r^2-38r+37)z^6 \\
& +4(r+1)^2(35r^3-324r^2+327r-82)z^5 \\
& -8(r+1)(6r^3+75r^2+136r-93)z^4 \\
& -16(18r^4+25r^3-104r^2+61r+44)z^3 \\
& -16(36r^3-23r^2-214r-115)z^2 + 384(3r^2+r-1)z + 2304r \Big] \\
& \times \frac{8(1-z)}{27(r+1)^2 z\left[z(r-1)+2\right]\left[z^2(r+1)^2-4\right]^2} \,,
\end{aligned}
\tag{34}
$$

$$
\begin{aligned}
\mathcal{F}_{gq}^{[10]}(z,r) \;=\; & \Big[ (r+1)(r^2-6r+1)z^2 - (r-1)(r^2+10r+1)z \\
& -2(r^2-2r-11) \Big] \frac{320z^3\ln(z)}{27\left[(r+1)z-2\right]^2\left[(r+1)z+2\right]^3} \\
& -\Big[ (r+1)^5 z^4 + 2(r+1)(3r^3+9r^2-23r+3)z^3 \\
& +4(r^3-21r^2+3r-7)z^2 - 8(r^2+6r-11)z - 64 \Big] \\
& \times \frac{40z^2\ln\left(1+2\frac{1-z}{z(r+1)}\right)}{27\left[(r+1)z-2\right]^2\left[(r+1)z+2\right]^3} \\
& +\Big[ (r-1)(r+1)^3 z^4 + 2(3r-1)(r^2-10r+5)z^3 + 4(3r^2-20r+9)z^2 \\
& +8(5r-7)z+64 \Big] \frac{80z(1-z)}{27\left[z(r-1)+2\right]\left[z^2(r+1)^2-4\right]^2} \,,
\end{aligned}
\tag{35}
$$

$$\mathcal{F}_{gq}^{[27_s]}(z,r) = \Big[r(r+1)z^2-(r-1)z-6\Big]\frac{16z^3(r+1)^2\ln(z)}{[(r+1)z-2]^2\,[(r+1)z+2]^3}$$
$$+\Big[(r+1)^4z^4-2(r+1)^2(3r-1)z^3-4(r+1)(r+5)z^2$$
$$+8(r+1)z-32\Big]\frac{2z^2(r+1)\ln\left(1+2\frac{1-z}{z(r+1)}\right)}{[(r+1)z-2]^2\,[(r+1)z+2]^3}$$
$$+\Big[(r+1)z^2+2(2r+1)z+8\Big]\frac{4z(1-z)(r+1)}{[z(r+1)+2]\,[z^2(r+1)^2-4]}\,, \qquad (36)$$

$$\mathcal{F}_{q\bar{q}}^{[1_s]}(z,r) = -\Big[18r^2(r^2+1)z^4+(81r^3-35r^2+27r-1)z^3+4(38r^2-13r+3)z^2$$
$$+4(31r-5)z+36\Big]\frac{8z\,[(9r+1)z+8]\ln\left(1+2\frac{1-z}{z(r+1)}\right)}{729(1-z)^2(rz+1)^3}$$
$$+\Big[18r^2(r^2-1)z^4+(81r^3+37r^2-27r+1)z^3+4(29r^2+14r-3)z^2$$
$$+2(35r+11)z+16\Big]\frac{16\,[(9r+1)z+8]}{729(r+1)(1-z)\,[(r-1)z+2]\,(rz+1)^2}\,, \qquad (37)$$

$$\mathcal{F}_{q\bar{q}}^{[8_s]}(z,r) = -\Big[9r^2(9r+4)(r^2+1)z^5+(477r^4+18r^3+130r^2+36r-13)z^4$$
$$+(1143r^3-44r^2+125r+52)z^3+2(668r^2-53r-1)z^2$$
$$+2(391r-14)z+180\Big]\frac{32z\ln\left(1+2\frac{1-z}{z(r+1)}\right)}{729(1-z)^2(rz+1)^3}$$
$$+\Big[9r^2(r^2-1)(9r+4)z^5+(477r^4+342r^3-104r^2-36r+13)z^4$$
$$+(981r^3+640r^2-73r-52)z^3+2(479r^2+253r+14)z^2$$
$$+40(11r+3)z+80\Big]\frac{64}{729(r+1)(1-z)\,[(r-1)z+2]\,(rz+1)^2}\,, \qquad (38)$$

$$
\begin{aligned}
\mathcal{F}_{q\overline{q}}^{[8_a]}(z,r) \;=\; & \Big[ 2r^3(9r^4+35r^3+41r^2-19r-2)z^6 \\
& +(88r^6+264r^5+309r^4-146r^3-26r^2-2r+1)z^5 \\
& +2r(104r^4+213r^3+271r^2-65r-3)z^4 \\
& +(349r^4+386r^3+492r^2-58r-1)z^3+4(99r^3+52r^2+63r-2)z^2 \\
& +2(125r^2+26r+29)z+64r\Big] \frac{\ln\left(1+2\frac{1-z}{z(r+1)}\right)}{12(r-1)^2(1-z)^2(rz+1)^3} \\
& -\Big[ 2r^2(r-1)(9r^3+35r^2+35r-3)z^5 \\
& +(88r^5+200r^4+129r^3-191r^2+15r-1)z^4 \\
& +2(107r^4+125r^3+140r^2-91r+3)z^3 \\
& +(329r^3+165r^2+215r-53)z^2+2(141r^2+54r+25)z \\
& +48(2r+1)\Big] \frac{1}{6(r-1)^2(1-z)\left[(r-1)z+2\right](rz+1)^2}\,,
\end{aligned} \tag{39}
$$

$$
\begin{aligned}
\mathcal{F}_{q\overline{q}}^{[10]}(z,r) \;=\; & \Big[ 8r^4z^4-(r^4-22r^3+6r-1)z^3-2(r^3-13r^2-5r+1)z^2 \\
& +16rz+8\Big] \frac{160z^2\ln\left(1+2\frac{1-z}{z(r+1)}\right)}{81(1-z)^2(rz+1)^3} \\
& -\Big[ 8r^2(r-1)z^3-(r^3-23r^2+9r+1)z^2-2(r^2-12r+3)z \\
& -2(r-7)\Big] \frac{320z^2}{81(1-z)\left[(r-1)z+2\right](rz+1)^2}\,,
\end{aligned} \tag{40}
$$

$$
\begin{aligned}
\mathcal{F}_{q\overline{q}}^{[27_s]}(z,r) \;=\; & -\Big[ 2r^2(r^2+1)z^4+(3r^2+1)(3r-1)z^3+4(4r^2-r+1)z^2 \\
& +4(3r-1)z+4\Big] \frac{8z^2(r+1)\ln\left(1+2\frac{1-z}{z(r+1)}\right)}{3(1-z)^2(rz+1)^3} \\
& +\Big[ 2r^2(r-1)z^3+(9r^2-4r+1)z^2+4(3r-1)z+6\Big] \\
& \times \frac{16z^2(r+1)}{3(1-z)\left[(r-1)z+2\right](rz+1)^2}\,.
\end{aligned} \tag{41}
$$

| benchmark point | SPS scenario | $m_0$ [GeV] | $m_{1/2}$ [GeV] | $A_0$ [GeV] | $\tan(\beta)$ | sign($\mu$) |
|---|---|---|---|---|---|---|
| (a) | SPS1a-point | 100 | 250 | $-100$ | 10 | 1 |
| (b) | SPS1a-slope1 | 80 | 200 | $-80$ | 10 | 1 |
| (c) | SPS1a-slope2 | 60 | 150 | $-60$ | 10 | 1 |
| (d) | SPS1a-slope3 | 120 | 300 | $-120$ | 10 | 1 |
| (e) | SPS1a-slope4 | 140 | 350 | $-140$ | 10 | 1 |
| (f) | SPS1a-slope5 | 160 | 400 | $-160$ | 10 | 1 |
| (g) | SPS1a-slope6 | 180 | 450 | $-180$ | 10 | 1 |
| (h) | SPS1a-slope7 | 200 | 500 | $-200$ | 10 | 1 |
| (i) | SPS1b-point | 200 | 400 | 0 | 30 | 1 |
| (j) | SPS2-point | 1450 | 300 | 0 | 10 | 1 |
| (k) | SPS2-slope1 | 1250 | 200 | 0 | 10 | 1 |
| (l) | SPS2-slope2 | 1050 | 100 | 0 | 10 | 1 |
| (m) | SPS2-slope3 | 1650 | 400 | 0 | 10 | 1 |
| (n) | SPS2-slope4 | 1850 | 500 | 0 | 10 | 1 |
| (o) | SPS3-point | 90 | 400 | 0 | 10 | 1 |
| (p) | SPS4-point | 400 | 300 | 0 | 50 | 1 |
| (q) | SPS5-point | 150 | 300 | $-1000$ | 5 | 1 |

Table 5: Initial parameters for the SPS scenarios to obtain the benchmark points.

# C Benchmark scenarios

This Appendix contains detailed information about the scenarios (a)-(q). The values of the `msugra` parameters defining the scenarios are listed in Tab. 5. In Tabs. 6 and 7 we list the values for the squark masses as provided by `SuSpect` [34]. Note that for our analysis the averaged values as provided in Tab. 3 are used.

# References


[1] H. Baer, V. Barger, A. Lessa and X. Tata, JHEP **0909** (2009) 063 [arXiv:0907.1922 [hep-ph]].

[2] P. R. Harrison and C. H. Llewellyn Smith, Nucl. Phys. B **213** (1983) 223 [Erratum-ibid. B **223** (1983) 542].

[3] H. E. Haber and G. L. Kane, Phys. Rept. **117**, 75 (1985).

[4] S. Dawson, E. Eichten and C. Quigg, Phys. Rev. D **31** (1985) 1581.

| benchmark point | $m_{\tilde{d}_1}$ [GeV] | $m_{\tilde{d}_2}$ [GeV] | $m_{\tilde{u}_1}$ [GeV] | $m_{\tilde{u}_2}$ [GeV] | $m_{\tilde{s}_1}$ [GeV] | $m_{\tilde{s}_2}$ [GeV] |
|---|---|---|---|---|---|---|
| (a) | 567.77 | 545.62 | 562.26 | 545.89 | 567.77 | 545.62 |
| (b) | 464.72 | 446.20 | 457.94 | 445.62 | 464.72 | 446.20 |
| (c) | 360.24 | 344.94 | 351.37 | 343.26 | 360.24 | 344.94 |
| (d) | 669.23 | 643.23 | 664.59 | 644.23 | 669.23 | 643.23 |
| (e) | 769.54 | 739.52 | 765.52 | 741.20 | 769.54 | 739.52 |
| (f) | 868.90 | 834.78 | 865.36 | 837.09 | 868.90 | 834.78 |
| (g) | 967.33 | 929.03 | 964.15 | 931.94 | 967.33 | 929.03 |
| (h) | 1065.22 | 1022.71 | 1062.35 | 1026.20 | 1065.23 | 1022.71 |
| (i) | 876.84 | 843.16 | 873.27 | 845.41 | 876.84 | 843.16 |
| (j) | 1556.70 | 1552.46 | 1554.76 | 1552.07 | 1556.70 | 1552.46 |
| (k) | 1300.76 | 1300.38 | 1298.41 | 1299.46 | 1300.76 | 1300.38 |
| (l) | 1055.59 | 1058.08 | 1052.65 | 1056.68 | 1055.59 | 1058.08 |
| (m) | 1817.49 | 1808.85 | 1815.83 | 1809.03 | 1817.49 | 1808.85 |
| (n) | 2080.64 | 2067.30 | 2079.20 | 2068.06 | 2080.64 | 2067.30 |
| (o) | 858.66 | 824.01 | 855.07 | 826.36 | 858.66 | 824.01 |
| (p) | 764.91 | 743.68 | 760.88 | 744.40 | 764.91 | 743.68 |
| (q) | 678.15 | 652.40 | 673.86 | 653.45 | 678.15 | 652.40 |

Table 6: $\tilde{d}$, $\tilde{u}$, $\tilde{s}$ masses for the various scenarios.

| benchmark point | $m_{\tilde{c}_1}$ [GeV] | $m_{\tilde{c}_2}$ [GeV] | $m_{\tilde{b}_1}$ [GeV] | $m_{\tilde{b}_2}$ [GeV] | $m_{\tilde{t}_1}$ [GeV] | $m_{\tilde{t}_2}$ [GeV] |
|---|---|---|---|---|---|---|
| (a) | 562.26 | 545.89 | 516.91 | 546.24 | 399.73 | 586.53 |
| (b) | 457.94 | 445.62 | 421.76 | 448.10 | 319.81 | 499.59 |
| (c) | 351.37 | 343.26 | 325.09 | 348.45 | 242.07 | 413.19 |
| (d) | 664.59 | 644.23 | 610.48 | 642.77 | 479.61 | 673.26 |
| (e) | 765.52 | 741.20 | 702.91 | 738.14 | 559.00 | 759.85 |
| (f) | 865.36 | 837.09 | 794.42 | 832.56 | 637.74 | 846.32 |
| (g) | 964.15 | 931.94 | 885.04 | 926.03 | 715.69 | 932.52 |
| (h) | 1062.35 | 1026.20 | 975.15 | 1018.98 | 793.11 | 1018.75 |
| (i) | 873.27 | 845.41 | 777.67 | 826.04 | 661.71 | 839.81 |
| (j) | 1554.76 | 1552.07 | 1298.73 | 1539.74 | 970.87 | 1307.45 |
| (k) | 1298.41 | 1299.46 | 1073.69 | 1289.26 | 789.69 | 1083.38 |
| (l) | 1052.65 | 1056.68 | 860.37 | 1048.57 | 622.94 | 870.89 |
| (m) | 1815.83 | 1809.03 | 1528.82 | 1794.54 | 1157.84 | 1536.48 |
| (n) | 2079.20 | 2068.06 | 1761.18 | 2051.40 | 1347.10 | 1767.83 |
| (o) | 855.07 | 826.36 | 792.13 | 822.99 | 649.29 | 842.40 |
| (p) | 760.88 | 744.40 | 617.79 | 685.28 | 546.52 | 696.19 |
| (q) | 673.86 | 653.45 | 561.85 | 650.48 | 248.72 | 649.57 |

Table 7: $\tilde{c}$, $\tilde{b}$, $\tilde{t}$ masses for the various scenarios.

[5] W. Beenakker, R. Höpker, M. Spira and P. M. Zerwas, Nucl. Phys. B **492** (1997) 51 [arXiv:hep-ph/9610490].

[6] W. Beenakker, R. Höpker and M. Spira, arXiv:hep-ph/9611232.

[7] W. Beenakker, M. Krämer, T. Plehn, M. Spira and P. M. Zerwas, Nucl. Phys. B **515** (1998) 3 [arXiv:hep-ph/9710451].

[8] A. Kulesza and L. Motyka, Phys. Rev. Lett. **102** (2009) 111802 [arXiv:0807.2405 [hep-ph]].

[9] U. Langenfeld and S. O. Moch, Phys. Lett. B **675** (2009) 210 [arXiv:0901.0802 [hep-ph]].

[10] A. Kulesza and L. Motyka, Phys. Rev. D **80** (2009) 095004 [arXiv:0905.4749 [hep-ph]].

[11] W. Beenakker, S. Brensing, M. Krämer, A. Kulesza, E. Laenen and I. Niessen, JHEP **0912**, 041 (2009) [arXiv:0909.4418 [hep-ph]].

[12] W. Beenakker, S. Brensing, M. Krämer, A. Kulesza, E. Laenen and I. Niessen, JHEP **1008**, 098 (2010) [arXiv:1006.4771 [hep-ph]].

[13] M. Beneke, P. Falgari, C. Schwinn, Nucl. Phys. **B842** (2011) 414. [arXiv:1007.5414 [hep-ph]].

[14] W. Beenakker, S. Brensing, M. Krämer, A. Kulesza, E. Laenen, L. Motyka and I. Niessen, Int. J. Mod. Phys. A **26** (2011) 2637 [arXiv:1105.1110 [hep-ph]].

[15] J. H. Kühn and E. Mirkes, Phys. Rev. D **48**, 179 (1993) [arXiv:hep-ph/9301204].

[16] W. Y. Keung and A. Khare, Phys. Rev. D **29**, 2657 (1984).

[17] J. H. Kühn and S. Ono, Phys. Lett. B **142**, 436 (1984).

[18] J. T. Goldman and H. Haber, Physica **15D**, 181 (1985).

[19] J. H. Kühn and P. M. Zerwas, Phys. Rept. **167**, 321 (1988).

[20] V. G. Kartvelishvili, A. V. Tkabladze and E. G. Chikovani, Z. Phys. C **43** (1989) 509.

[21] V. G. Kartvelishvili, A. V. Tkabladze and E. G. Chikovani, Sov. J. Nucl. Phys. **51**, 546 (1990) [Yad. Fiz. **51**, 859 (1990)].

[22] E. Chikovani, V. Kartvelishvili, R. Shanidze and G. Shaw, Phys. Rev. D **53**, 6653 (1996) [arXiv:hep-ph/9602249].

[23] G. F. Giudice and A. Romanino, Nucl. Phys. B **699**, 65 (2004) [Erratum-ibid. B **706**, 65 (2005)] [arXiv:hep-ph/0406088].

[24] N. Arkani-Hamed and S. Dimopoulos, JHEP **0506**, 073 (2005) [arXiv:hep-th/0405159].

[25] W. Kilian, T. Plehn, P. Richardson and E. Schmidt, Eur. Phys. J. C **39**, 229 (2005) [arXiv:hep-ph/0408088].

[26] K. Cheung and W. Y. Keung, Phys. Rev. D **71**, 015015 (2005) [arXiv:hep-ph/0408335].

[27] M. R. Kauth, J. H. Kühn, P. Marquard and M. Steinhauser, Nucl. Phys. B **831** (2010) 285 [arXiv:0910.2612 [hep-ph]].

[28] K. Hagiwara, Y. Sumino and H. Yokoya, Phys. Lett. B **666**, 71 (2008) [arXiv:0804.1014 [hep-ph]].

[29] Y. Kiyo, J. H. Kühn, S. Moch, M. Steinhauser and P. Uwer, Eur. Phys. J. C **60** (2009) 375 [arXiv:0812.0919 [hep-ph]].

[30] K. Hagiwara and H. Yokoya, JHEP **0910** (2009) 049 [arXiv:0909.3204 [hep-ph]].

[31] A. Petrelli, M. Cacciari, M. Greco, F. Maltoni and M. L. Mangano, Nucl. Phys. B **514** (1998) 245 [arXiv:hep-ph/9707223].

[32] A. J. MacFarlane, A. Sudbery and P. H. Weisz, Commun. Math. Phys. **11** (1968) 77.

[33] B. C. Allanach *et al.*, in *Proc. of the APS/DPF/DPB Summer Study on the Future of Particle Physics (Snowmass 2001)* ed. N. Graf, Eur. Phys. J. C **25** (2002) 113 [arXiv:hep-ph/0202233].

[34] A. Djouadi, J. L. Kneur and G. Moultaka, Comput. Phys. Commun. **176** (2007) 426 [arXiv:hep-ph/0211331].

[35] M. Mühlleitner, A. Djouadi and Y. Mambrini, Comput. Phys. Commun. **168**, 46 (2005) [arXiv:hep-ph/0311167].

[36] M. Beneke, P. Falgari, C. Schwinn, Nucl. Phys. **B828** (2010) 69. [arXiv:0907.1443 [hep-ph]].

[37] J. Bartels, Z. Phys. C **60** (1993) 471.

[38] A. D. Martin, W. J. Stirling, R. S. Thorne and G. Watt, arXiv:0901.0002 [hep-ph].

[39] K. G. Chetyrkin, J. H. Kühn, M. Steinhauser, Comput. Phys. Commun. **133** (2000) 43-65. [hep-ph/0004189].

[40] R. V. Harlander, L. Mihaila and M. Steinhauser, Phys. Rev. D **76** (2007) 055002 [arXiv:0706.2953 [hep-ph]].

[41] V. S. Fadin and V. A. Khoze, JETP Lett. **46**, 525 (1987) [Pisma Zh. Eksp. Teor. Fiz. **46**, 417 (1987)].

[42] V. S. Fadin and V. A. Khoze, Sov. J. Nucl. Phys. **48** (1988) 309 [Yad. Fiz. **48** (1988) 487].

[43] V. S. Fadin, V. A. Khoze and T. Sjöstrand, Z. Phys. C **48**, 613 (1990).

[44] A. V. Smirnov, V. A. Smirnov and M. Steinhauser, Phys. Rev. Lett. **104** (2010) 112002 [arXiv:0911.4742 [hep-ph]].

[45] A. V. Smirnov, V. A. Smirnov and M. Steinhauser, Phys. Lett. B **668** (2008) 293 [arXiv:0809.1927 [hep-ph]].

[46] C. Anzai, Y. Kiyo and Y. Sumino, Phys. Rev. Lett. **104** (2010) 112003 [arXiv:0911.4335 [hep-ph]].

[47] C. Anzai, Y. Kiyo and Y. Sumino, Nucl. Phys. B **838** (2010) 28 [arXiv:1004.1562 [hep-ph]].

[48] B. A. Kniehl, A. A. Penin, Y. Schröder, V. A. Smirnov and M. Steinhauser, Phys. Lett. B **607** (2005) 96 [arXiv:hep-ph/0412083].

[49] M. Beneke, A. Signer and V. A. Smirnov, Phys. Lett. B **454** (1999) 137 [arXiv:hep-ph/9903260].

[50] A. Pineda and A. Signer, Nucl. Phys. B **762** (2007) 67 [arXiv:hep-ph/0607239].

[51] M. Beneke, Y. Kiyo and K. Schuller, Nucl. Phys. B **714**, 67 (2005) [arXiv:hep-ph/0501289].

[52] T. Hahn, Comput. Phys. Commun. **140** (2001) 418-431. [hep-ph/0012260].

[53] T. Hahn, C. Schappacher, Comput. Phys. Commun. **143** (2002) 54-68. [hep-ph/0105349].

[54] J. A. M. Vermaseren, [math-ph/0010025].

[55] W. Siegel, Phys. Lett. B **84** (1979) 193.

[56] S. P. Martin and M. T. Vaughn, Phys. Lett. B **318** (1993) 331 [arXiv:hep-ph/9308222].

[57] L. Mihaila, Phys. Lett. B **681** (2009) 52 [arXiv:0908.3403 [hep-ph]].

[58] J. H. Kühn, J. Kaplan and E. G. O. Safiani, Nucl. Phys. B **157**, 125 (1979).

[59] B. Guberina, J. H. Kühn, R. D. Peccei and R. Rückl, Nucl. Phys. B **174**, 317 (1980).

[60] M. R. Kauth, PhD Thesis, KIT.

[61] T. Huber and D. Maitre, Comput. Phys. Commun. **175** (2006) 122 [arXiv:hep-ph/0507094].

[62] G. 't Hooft and M. J. G. Veltman, Nucl. Phys. B **153**, 365 (1979).